Parity violating non-Gaussianity from axion-gauge field dynamics

Ogan Özsoy
CEICO, Institute of Physics of the Czech Academy of Sciences, Na Slovance 1999/2, 182 21, Prague

(Received 18 July 2021; accepted 9 November 2021; published 20 December 2021)

We study scalar-tensor-tensor and tensor-scalar-scalar three-point cross-correlations generated by the dynamics of a transiently rolling spectator axion-U(1) gauge field model during inflation. In this framework, tensor and scalar fluctuations are sourced by gauge fields at the nonlinear level due to gravitational interactions, providing a chiral background of gravitational waves while keeping the level of scalar fluctuations at the observationally viable levels at cosmic microwave background (CMB) scales. We show that the gravitational couplings between the observable sector and gauge fields can also mediate strong correlations between scalar and tensor fluctuations, generating an amplitude for the mixed-type three-point functions that is parametrically larger—$f_{\rm NL} \simeq \mathcal{O}(1-10)(r/0.01)^{3/2}$—compared to the single-field realizations of inflation. As the amplification of the gauge field sources are localized around the time of horizon exit, the resulting mixed bispectra are peaked *close* to the equilateral configurations. The shape dependence along with the scale dependence and the parity violating nature of the mixed bispectra can serve as a distinguishing feature of the underlying axion-gauge field dynamics and suggest a careful investigation of their signatures on the CMB observables including cross-correlations between temperature T and E,B polarization modes.

DOI: 10.1103/PhysRevD.104.123523

I. INTRODUCTION

The production of primordial gravitational waves (GWs) (see, e.g., reviews [1,2]) is a robust prediction of the inflationary paradigm [3–5]. A positive detection of such fossil GWs would therefore provide strong evidence for inflation in the early Universe. The amplitude of this signal is conventionally parametrized by the so-called tensor-to-scalar ratio r which is a quantity targeted by a number of probes aiming to observe B-mode polarization patterns [6,7] in the cosmic microwave background (CMB) sky [8]. Current limits on the tensor-to-scalar ratio from Planck and BICEP/Keck restrict $r \lesssim 0.06$ [9,10] and are expected to be improved by an order of magnitude by the forthcoming experiments such as CMB-S4 [11] and LiteBIRD [12].

In simplest realizations of inflation based on a scalar field minimally coupled to Einstein gravity, primordial GWs originate from the quantum vacuum fluctuations of the metric amplified by the quasi–de Sitter (quasi-dS) expansion. In this framework, the amplitude of the produced GWs is directly related to the expansion rate $H_{\rm inf}$ of the quasi-dS background, and thus, if GWs are observed, they would provide us the energy scale of inflation $H_{\rm inf} \sim 10^{-5}(r/0.01)^{1/2} M_{\rm pl}$ and give us the first hints on the quantum nature of gravity. More importantly, in this setup, the resulting GW signal is expected to posses the following properties: (i) near-scale invariance (with a slight red tilt), (ii) near Gaussianity, and (iii) parity conservation.[1] In order to have a firm understanding of the fundamental nature of inflation, it is therefore crucial to test the robustness of these predictions by exploring viable alternative mechanisms that can generate GWs during inflation.

In fact, the properties (i)–(iii) of tensor fluctuations do not generically hold and can be invalidated if additional energetic enough field configurations present during inflation (see, e.g., [17,18]). From a top-down model-building perspective, a rich particle content during inflation is not just an interesting possibility but appears to be a common outcome of many theories beyond the Standard Model of particle physics (see, e.g., [19]). For example, low energy effective descriptions of string theory and supergravity generically predict a plethora of scalar fields (moduli or axionlike fields) along with gauge sectors that interact with each other at the nonlinear level through dilaton or Chern-Simons-like couplings.[2] In the presence of such couplings,

---

[1] Within the generalized scalar-tensor theories of single-field inflation, a blue-tilted tensor spectrum can be generated for backgrounds that exhibit a transient nonattractor era [13,14]. On the other hand, parity violation in the tensor sector can be induced by nonminimal couplings between inflaton and the metric [15,16].

[2] The phenomenological roles played by these couplings are initially considered in the context of primordial magnetogenesis [20,21] and more recently to realize axion inflation with sub-Planckian decay constants, e.g., through strong dissipative dynamics induced by U(1) [22] or SU(2) [23] gauge sectors. For explicit embeddings of the SU(2) model in supergravity and string theory constructions, see [24] and [25,26], respectively.

the classical role of the scalar background fields can "lift" the gauge field fluctuations and enhance their amplitude during inflation in a parity violating manner. Produced gauge field modes in this way then can influence the observed tensor fluctuations and can generate a large "synthetic" component of *chiral* GWs. However, for vector fields that exhibit direct coupling with the observable scalar sector, this is a challenging task because the induced GW emission is also accompanied by the strong production of non-Gaussian scalar fluctuations [27–30] which puts a bound on the size of the sourced GW component at CMB scales[3] [38,39].

To resolve this tension, an extension of these models is proposed that utilizes a spectator axion-U(1) gauge sector endowed with localized gauge field production [40,41]. In this framework, the model is equipped with an additional scalar field that drives inflation and controls observable fluctuations in the scalar sector.[4] Armed with this property and thanks to the localized nature of gauge field production, scalar fluctuations in this model can be kept in observationally viable levels while keeping its original intriguing features such as the generation of chiral GWs of nonvacuum origin. Remarkably, a scan of the parameter space in these models shows that the parity violating tensor power spectrum reveals that such a signal may be observable through the mixed angular power spectra[5] of the CMB temperature T anisotropies and E,B polarization modes [40].

In these models, intriguing parity violating signatures of tensor fluctuations also appear in the tensor-tensor-tensor correlator. In particular, a sizeable scale-dependent tensor non-Gaussianity can be induced by the amplified gauge field fluctuations [40,41] and the parity violation associated with $\langle h_\lambda h_\lambda h_\lambda \rangle$ can reveal itself in the CMB bispectrum of B modes [51]. Since scalar fluctuations are also enhanced to a certain extent by the gauge fields, it is then natural to ask if there exist three-point cross-correlations between scalar and tensor fluctuations. In the spectator axion-U(1) gauge field models, we expect such mixed correlations to appear on the following grounds: First of all, as we mentioned before, the transient instability in the vector fields can directly influence the metric fluctuations through the inevitable cubic gravitational interaction of hAA type. On the other hand, the scalar fluctuations $\delta\phi$ in the observable inflaton sector can linearly mix with the scalar fluctuations in the spectator axion sector which have direct cubic interactions of σAA type with the gauge field modes. Therefore, mediated by the Abelian vector fields, a bridge between the comoving curvature perturbation $\mathcal{R} \propto \delta\phi$ and tensor fluctuations h can be built to induce scalar-tensor-tensor $\mathcal{R}hh$-type and tensor-scalar-scalar $h\mathcal{R}\mathcal{R}$-type mixed three-point correlators (see Fig. 2).

Considering the preferred handedness of tensor fluctuations, along with the scale dependence and the non-Gaussian nature of the cosmological fluctuations in these models, a detailed analysis of the mixed bispectra of tensor and scalar perturbations could provide us invaluable information on their underlying production mechanism and guide us to compare these predictions with that of the conventional single-field models, as well as other nonconventional scenarios.[6] Therefore, for a complete understanding of parity violating signatures in the spectator axion-U(1) gauge field models [40,41], it is timely to consider three-point cross-correlations between scalar and tensor fluctuations which is the main focus of this work.

This paper is organized as follows: In Sec. II, we review the transiently rolling spectator axion-gauge field model and its predictions at the level of power and autobispectra. In Sec. III, we present our results on the scalar-tensor-tensor and tensor-scalar-scalar bispectrum and discuss their amplitude and shape dependence. We conclude in Sec. IV. We supplement our results with five Appendixes where many details about the computations we carry out can be found.

Notations and conventions: Our metric signature is mostly plus sign $(-,+,+,+)$. Greek indices stand for space-time coordinates, while latin indices denote spatial coordinates. Overdots and primes on time-dependent quantities denote derivatives with respect to coordinate time t and conformal time τ, respectively. At leading order in slow-roll parameters, we take the scale factor as $a(\tau) = 1/(-H\tau)$ where $H = \dot{a}/a$ is the physical Hubble rate during inflation.

II. COSMOLOGICAL FLUCTUATIONS FROM AXION-GAUGE FIELD DYNAMICS

As we mentioned in the Introduction, the Lagrangian that describes the model contains an inflationary sector together with a spectator axion-gauge field sector both minimally coupled to gravity [40–42,56],

$$\frac{\mathcal{L}}{\sqrt{-g}} = \frac{M_{\rm pl}^2 R}{2} + \mathcal{L}_\phi \underbrace{- \frac{1}{2}(\partial\sigma)^2 - V_\sigma(\sigma) - \frac{1}{4}F_{\mu\nu}F^{\mu\nu} - \frac{\alpha_c \sigma}{4f}F_{\mu\nu}\tilde{F}^{\mu\nu}}_{\text{Spectator sector}}, \tag{2.1}$$

---

[3] At sub-CMB scales, however, the same mechanism can be utilized to obtain sufficient enhancement in the scalar fluctuations required for primordial black hole production [31–37].

[4] For early studies of the spectator axion-U(1) gauge field model, see [42,43]; for a discussion on the issues regarding the scalar fluctuations in this model, see [44,45].

[5] For earlier studies of probing chiral GWs with CMB anisotropies, see [46–50].

[6] See, e.g., [52,53] for an analysis of mixed bispectrum of scalar and tensor fluctuations in the spectator axion-SU(2) gauge field model. On the other hand, parity violating $\langle \mathcal{R}hh \rangle$ bispectrum can also arise through the gravitational Chern-Simons-type coupling to the inflation; see, e.g., [54,55] for the detectability of this signal through TBB and EBB CMB bispectra, respectively.

where $\mathcal{L}_\phi$ is the Lagrangian that drives inflation and is responsible for the generation of curvature perturbation consistent with CMB observations, and σ is a spectator pseudo-scalar axion rolling on its potential V_σ. The strength of the interaction [i.e., the last term in (2.1)] between the spectator σ and the gauge field is parametrized by the scale f together with the dimensionless coupling constant α_c where $F_{\mu\nu} = \partial_\mu A_\nu - \partial_\nu A_\mu$ is the field strength tensor of the U(1) gauge field, $\tilde{F}^{\mu\nu} \equiv \eta^{\mu\nu\rho\sigma} F_{\rho\sigma}/(2\sqrt{-g})$ is its dual, and alternating symbol $\eta^{\mu\nu\rho\sigma}$ is 1 for even permutation of its indices, -1 for odd permutations, and zero otherwise.

A. Gauge field production

If the spectator axion rolls on its potential V_σ with a nonvanishing background velocity $\dot{\sigma} \neq 0$, the interaction in (2.1) introduces a tachyonic mass for the gauge field and leads to the enhancement of gauge field modes in a parity violating manner. This can be seen from the equation of motion of the gauge field polarization states $A_\pm$ in a Friedmann-Robertson-Walker background [22],

$$\left(\partial_x^2 + 1 \pm \frac{aH}{k} 2\xi\right) A_\pm = 0, \tag{2.2}$$

where we defined $x \equiv -k\tau$ and $\xi \equiv -\alpha_c \dot{\sigma}/(2Hf)$ ($\xi > 0 \,\&\, \dot{\sigma} < 0$) is the dimensionless measure of the axion's velocity that represents the effective coupling strength between σ and A_μ. From (2.2), we see that when the last term dominates over unity for $k/(aH) < 2\xi$, only the $-$ polarization state of the gauge field experiences tachyonic instability which reflects the parity violating nature of the $\sigma F\tilde{F}$ interaction.

B. Tensors sourced by vector fields

The gauge field fluctuations produced in this way exhibit an amplitude $A_- \propto e^{\pi\xi}$ [22], which in turn acts as an additional source of tensor perturbations through gravitational interactions [42]. This can be seen clearly from the mode equation of graviton polarization states h_λ which is sourced by the transverse traceless part of the energy-momentum tensor composed of gauge field fluctuations:

$$\left(\partial_\tau^2 + k^2 - \frac{2}{\tau^2}\right)(a\hat{h}_\lambda) = -\frac{2a^3}{M_{\rm pl}^2} \Pi_{ij,\lambda}(\vec{k}) \int \frac{{\rm d}^3 p}{(2\pi)^{3/2}} [\hat{E}_i(\tau, \vec{k}-\vec{p})\hat{E}_j(\tau,\vec{p}) + \hat{B}_i(\tau,\vec{k}-\vec{p})\hat{B}_j(\tau,\vec{p})], \tag{2.3}$$

where $\hat{E}_i = -a^{-2}\hat{A}_i'$, $\hat{B}_i = a^{-2}\epsilon_{ijk}\partial_j \hat{A}_k$ are "electric" and "magnetic" fields, and $\hat{h}_\lambda(\tau,\vec{k}) = \Pi_{ij,\lambda}(\vec{k})\hat{h}_{ij}(\tau,\vec{k})$ with $\Pi_{ij,\lambda}$ being the polarization tensor obeying $\hat{k}_i \Pi_{ij,\lambda}(\vec{k}) = 0$, $\Pi^*_{ij,\lambda}\Pi_{ij,\lambda'} = \delta_{\lambda\lambda'}$ and $\Pi^*_{ij,\lambda}(\vec{k}) = \Pi_{ij,-\lambda}(\vec{k}) = \Pi_{ij,\lambda}(-\vec{k})$.

C. Scalars sourced by vector fields

The influence of particle production on the visible scalar sector is also encoded indirectly by the presence of gravitational interactions [44]. In particular, integrating out the nondynamical lapse δN and the shift N^i reveals a mass mixing between $\delta\phi$ and $\delta\sigma$ and opens up a channel that can influence the curvature perturbation[7] $\mathcal{R} \simeq -H\delta\phi/\dot{\phi}$ through the inverse decay of gauge fields: $A_i + A_i \to \delta\sigma \to \delta\phi \propto \mathcal{R}$. Dynamics of this contribution can be understood by first studying the influence of particle production on the spectator fluctuations $\delta\sigma$ through

$$\left(\frac{\partial^2}{\partial\tau^2} + k^2 - \frac{2}{\tau^2}\right)(a\delta\hat{\sigma}) \simeq a^3 \frac{\alpha_c}{f} \int \frac{{\rm d}^3 p}{(2\pi)^{3/2}} \hat{E}_i(\tau, \vec{k}-\vec{p})\hat{B}_i(\tau,\vec{p}). \tag{2.4}$$

Focusing on the inhomogeneous solution of the $\delta\sigma$ fluctuations in (2.4), one can then compute the conversion of the resulting $\delta\sigma$ to $\delta\phi$ via

$$\left(\frac{\partial^2}{\partial\tau^2} + k^2 - \frac{2}{\tau^2}\right)(a\delta\hat{\phi}) \simeq 3a^2 \frac{\dot{\phi}\dot{\sigma}}{M_{\rm pl}^2}(a\delta\hat{\sigma}) \tag{2.5}$$

to find the part of the curvature perturbation that is sourced by the amplified gauge fields.

It has recently been shown that if σ rolls for a large amount of time ($\Delta N_\sigma \gg 1$) during inflation, the sourced contributions to the $\mathcal{R}$ can be sizeable due to the sensitivity of gauge field amplitudes and $\delta\phi - \delta\sigma$ mixing on the spectator axion's velocity $\xi \propto |\dot{\sigma}|$ [44]. In particular, this would lead to an exceedingly large CMB non-Gaussianity, and once the CMB limits on it are respected, the sourced GW signal is bounded by $r < 10^{-3} - 10^{-4}$ at CMB scales [44,45]. To minimize the influence of the enhanced gauge fields on the curvature perturbation and to render

---

[7] In the multifield model we are considering, late-time $\mathcal{R}$ also obtains direct contributions from fluctuations linear in the spectator axion $\delta\sigma$ and the gauge fields at nonlinear order. For a spectator axion that rolls down to its minimum long before the end of inflation—as we assume in this work—the contribution of $\delta\sigma$ can be neglected [40,43]. The contribution from gauge fields, on the other hand, is roughly proportional to the absolute value of the Poynting vector $a|\vec{S}| = a|\vec{E}\times\vec{B}|$, which is also negligible at late times as the particle production saturates at superhorizon scales, and the resulting electromagnetic fields decay as $\vec{E},\vec{B} \sim a^{-2}$ [41]. For the purpose of evaluating mixed correlators, we therefore adopt the standard relation $\mathcal{R} \equiv -H\delta\phi/\dot{\phi}$ in this work.

observable GWs sourced by gauge fields viable, more realistic models that lead to localized gauge field production have been proposed where the spectator axion transiently rolls on potentials of the following form [40,41]:

$$V_\sigma(\sigma)=\begin{cases}\Lambda^4[1-\cos(\frac{\sigma}{f})], & \text{Model 1 (M1)},\\ \mu^3\sigma+\Lambda^4[1-\cos(\frac{\sigma}{f})]\;\&\;\Lambda^4\lesssim\mu^3 f, & \text{Model 2 (M2)}.\end{cases} \tag{2.6}$$

The first model (M1) features a spectator axion with standard shift symmetric potential (see, e.g., [57]) where the size of the axion modulations is set by the mass parameter Λ. In this model, the motion of the axion is contained within the maximum ($\sigma=\pi f$) and the minimum ($\sigma=0$) of the potential, whereas in the second model (M2), the axion field range is extended via a monodromy term [58,59] proportional to a second mass parameter μ, and σ is assumed to probe steplike feature(s) in the "bumpy" regime $\Lambda^4\lesssim\mu^3 f$.[8]

For the typical field ranges dictated by the scalar potentials (2.6) and assuming a slow-roll $\ddot\sigma\ll 3H\dot\sigma$ condition, the spectator field velocity $\dot\sigma$ and the effective coupling $\xi=-\alpha_c/(\dot\sigma/2Hf)$ in (2.2) obtain a peaked time-dependent profile given by [40,41]

$$\xi(\tau)=\begin{cases}\frac{2\xi_*}{(\tau_*/\tau)^\delta+(\tau/\tau_*)^\delta}, & \text{Model 1(M1)},\\ \frac{\xi_*}{1+\ln[(\tau/\tau_*)^\delta]^2}, & \text{Model 2(M2)},\end{cases} \tag{2.7}$$

where $\xi_*=\{\alpha_c\delta/2\,(\text{M1}),\alpha_c\delta\,(\text{M2})\}$ is the maximum value of ξ when the axion's velocity becomes maximal at the conformal time τ_*. In (2.7), we defined the dimensionless ratios $\delta=\Lambda^4/6H^2f^2$ (M1) and $\delta\simeq\mu^3/3H^2f$ (M2) in terms of the model parameters. Physically, δ is a measure for the acceleration $[\dot\xi/(\xi H)=\ddot\sigma/(\dot\sigma H)\sim\delta]$ of the spectator axion as it rolls down on its potential. Note that since the slow-roll approximation $\ddot\sigma\ll 3H\dot\sigma$ is assumed to derive (2.7), we require $\delta<1$. In this work, without loss of generality, we will adopt $\delta=0.3$[9] to derive phenomenological implications of spectator axion-gauge field dynamics.

As we review in Appendix A, the time-dependent profile (2.7) for ξ translates into a scale-dependent growth of the gauge fields in (2.2) where only modes that have a size comparable to the horizon, i.e., $k\simeq\mathcal{O}(1)a_*H_*$ at $\tau=\tau_*$, are efficiently amplified. Below, we review the impact of such a scale-dependent vector field production on the autocorrelators of tensor and scalar fluctuations during inflation.

D. Chiral GWs from gauge field sources

In the presence of gauge field amplification, the perturbations in the observable sector $\hat{\mathcal{X}}=\{\hat{\mathcal{R}},\hat{h}_\pm\}$ pick up a sourced contribution that can be described by the particular solutions of (2.3) and (2.5) [see also (2.4)] in addition to the vacuum counterpart generated by quasi-dS background: $\hat{\mathcal{X}}=\hat{\mathcal{X}}^{(\mathrm{v})}+\hat{\mathcal{X}}^{(s)}$. These contributions are statistically uncorrelated, and therefore, the total power spectra can be simply described by the sum of the vacuum and sourced part

$$\mathcal{P}_\mathcal{R}(k)=\mathcal{P}_\mathcal{R}^{(v)}(k)+\mathcal{P}_\mathcal{R}^{(s)}(k),\quad \mathcal{P}_\pm(k)=\mathcal{P}_\pm^{(v)}(k)+\mathcal{P}_\pm^{(s)}(k), \tag{2.8}$$

where the vacuum contributions are given by the standard expressions

$$\mathcal{P}_\mathcal{R}^{(v)}=\frac{H^2}{8\pi^2\epsilon_\phi M_{\mathrm{pl}}^2},\qquad \mathcal{P}_\pm^{(v)}=\frac{H^2}{\pi^2M_{\mathrm{pl}}^2}, \tag{2.9}$$

where $\epsilon_\phi\equiv\dot\phi^2/(2H^2M_{\mathrm{pl}}^2)$ is the slow-roll parameter controlled by the inflaton sector. On the other hand, the sourced power spectra in (2.8) inherits the scale dependence of the gauge field sources, which can be shown to acquire a Gaussian form [40,41]

$$\mathcal{P}_j^{(s)}(k)=[\epsilon_\phi\mathcal{P}_\mathcal{R}^{(v)}(k)]^2f_{2,j}\left(\xi_*,\frac{k}{k_*},\delta\right),$$
$$f_{2,j}\left(\xi_*,\frac{k}{k_*},\delta\right)\simeq f_{2,j}^c[\xi_*,\delta]\exp\left[-\frac{1}{2\sigma_{2,j}^2[\xi_*,\delta]}\times\ln^2\left(\frac{k}{k_*x_{2,j}^c[\xi_*,\delta]}\right)\right], \tag{2.10}$$

where $j=\{\mathcal{R},\pm\}$. The functions $f_{2,j}^c,\sigma_{2,j},x_{2,j}^c$ control, respectively, the amplitude, width, and position of the peak of the sourced signal, which depend on the background model of the spectator axion through the parameters ξ_* and δ that we discussed above and therefore to the underlying scalar potential (2.6) in the spectator axion sector. For a representative choice of the background parameter δ, we present accurate formulas for $f_{2,j}^c,\sigma_{2,j},x_{2,j}^c$ in terms of the effective coupling ξ_* in Table IV.

At this point, it is intriguing to ask if the gauge field sources can be sufficiently large to alter the tensor-to-scalar ratio defined by [40,41]

---

[8] In the bumpy regime, depending on the initial conditions ($\sigma\gg f$) the spectator axion can probe multiple steplike features during inflation. In this work, we assume that σ traverses only one such region on its potential, during which the observable scales associated with CMB exit the horizon.

[9] We note that this choice is not a unique requirement for successful phenomenology, and other values for δ can be adopted (see, e.g., [40]) as far as we restrict ourselves to $0\le\delta<1$. However, different choices of δ within this range influence the properties of the scale-dependent signals as we explain in Sec. III. For example, the $\delta\to 0$ limit corresponds to the standard scale invariant production of gauge fields (with a constant ξ) for an axion rolling at a constant rate [22,27]. We refer the reader to [40,41] for many details regarding the parameter δ including its relation with axion dynamics, particle production in the gauge field sector, and the resulting phenomenology of scalar and tensor correlators.

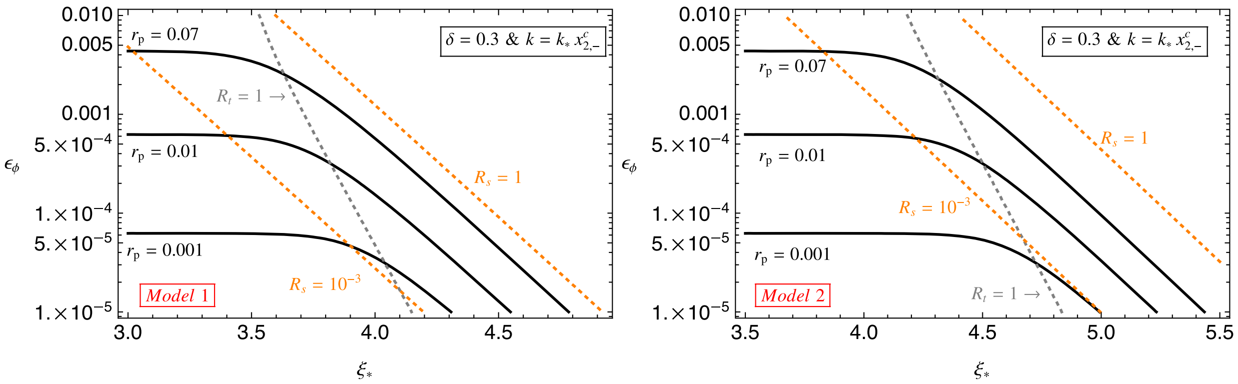

FIG. 1. Constant r curves in the $\epsilon_\phi - \xi_*$ plane for Model 1 (left) and Model 2 (right). Orange dotted (respectively, gray dotted) lines show the ratio between the sourced and the vacuum scalar (respectively, tensor) power spectrum R_s (R_t) (see Appendix B for details).

$$r(k) = \sum_\lambda \frac{\mathcal{P}_\lambda^{(v)}(k) + \mathcal{P}_\lambda^{(s)}(k)}{\mathcal{P}_\mathcal{R}^{(v)}(k) + \mathcal{P}_\mathcal{R}^{(s)}(k)}. \qquad (2.11)$$

To address this question, in Fig. 1 we show constant curves of tensor-to-scalar ratio r (2.11) evaluated at the peak of the sourced GW signal $r(k_p = k_* x^c_{2,-}) = r_p$ in the $\epsilon_\phi - \xi_*$ plane for both models (see Appendix B). In this plot, the region spanning between the $R_t \equiv \mathcal{P}_-^{(s)}/\mathcal{P}_h^{(v)} > 1$ and $R_s \equiv \mathcal{P}_\mathcal{R}^{(s)}/\mathcal{P}_\mathcal{R}^{(v)} \ll 1$ locates the parameter space where sourced GWs dominate over the vacuum fluctuations while keeping the amplitude of scalar fluctuations sourced by the gauge fields under control.[10] In this region, tensor-to-scalar ratio r acquires an exponential sensitivity to gauge field production [see (B3)], breaking the standard relation between r and H of single-field inflation. Excitingly, the GW signal produced by the gauge field sources is maximally chiral $\chi \equiv (\mathcal{P}_- - \mathcal{P}_+)/\sum_\lambda \mathcal{P}_\lambda \sim \mathcal{O}(1)$ (see, e.g., [60]), which is an essential distinguishing feature of the inflationary models we consider in this work.[11]

E. Scalar and tensor bispectrum

The scale-dependent amplification of gauge fields also influences three-point correlators of scalar and tensor perturbations. An immediate worry at this point is to keep the scalar bispectrum $\langle \hat{\mathcal{R}}_{k_1} \hat{\mathcal{R}}_{k_2} \hat{\mathcal{R}}_{k_3} \rangle$ below the CMB observational limits while preserving a large chiral GW signal from gauge field sources. This issue is addressed in [40,41] for both spectator axion-gauge field models where it was shown that stringent constraints on scalar non-Gaussianity at CMB scales can be avoided for much of the parameter space of these models, thanks to the localized nature of particle production in the gauge field sources. Remarkably, a sizeable parity violating tensor non-Gaussianity $\langle \hat{h}_{k_1} \hat{h}_{k_2} \hat{h}_{k_3} \rangle$[12] can also be generated by the gauge field sources, providing an opportunity to test these models through the CMB B-mode bispectrum [51].

For the distinguishability of these signals, shape-dependent three-point autocorrelators will provide further information. The shape analysis is carried out for the first model discussed [see M1 in (2.6)] [40], where it was shown that both bispectra are maximal at the equilateral configurations $k_1 \approx k_2 \approx k_3 \simeq \mathcal{O}(1-10)k_*$. In Appendix C, we likewise perform the shape analysis of the bispectra for the noncompact axion model (M2) in (2.6) to confirm that both scalar and tensor bispectra are also maximal at the equilateral configuration in this model. The appearance of the equilateral shape in the autocorrelators is closely tied to the gauge field sources which have maximal support only for modes satisfying $q \simeq \mathcal{O}(1) a_* H_*$ (see Table III).

Because of scale-dependent amplifications of tensor (T) and scalar (S) fluctuations, their three-point cross-correlations may also contain invaluable information on the production mechanism of primordial GWs and more importantly on the inflationary field content. Considering the chirality of the tensor fluctuations present in these

---

[10] In the $R_s \ll 1$ regime, additional limitations on the model parameter space arise from the CMB constraints on the spectral tilt and its running. For both models (M1, M2) we consider, a detailed discussion on these limitations appeared in [41,56] where it was found that axion decay constants that roughly obey $f/M_{\rm pl} < 0.1$ (at fixed δ) are preferred in order to grant observable GWs of nonvacuum origin. Note that this bound does not lead to an additional constraint on the amplitude of the signals sourced by the gauge fields as the latter mainly controlled by ξ_* or equivalently by the dimensionless coupling constant α_c at fixed δ, considering the relation $\xi_* \propto \alpha_c \delta$.

[11] In contrast to standard predictions of inflation, chiral GWs can produce a nonvanishing cross-correlation between CMB temperature (T) anisotropies and polarization modes (E,B) [46–48]. See, e.g., [40] for an analysis of the observability of the CMB TB correlator within the first model we present here. On the other hand, the observability of a chiral GW signal in the spectator axion-SU(2) gauge field model is studied in [61].

[12] Observably, large tensor non-Gaussianity can also arise from spectator axion-SU(2) gauge field dynamics during inflation [62,63].

models, the size and shape of the mixed non-Gaussianity is complementary to the autocorrelators of $\hat{\mathcal{R}}$ and $\hat{h}$ in extracting this unique information and can help us distinguish this class of models from other scenarios. In what follows, we will study the mixed non-Gaussianity of scalar-tensor-tensor $\langle\hat{\mathcal{R}}\hat{h}\hat{h}\rangle$ (STT) and tensor-scalar-scalar $\langle\hat{h}\hat{\mathcal{R}}\hat{\mathcal{R}}\rangle$ (TSS) types during inflation focusing on the spectator axion-gauge field dynamics described by the potentials (2.6).

III. MIXED NON-GAUSSIANITY FROM AXION-GAUGE FIELD DYNAMICS

In the theory described by the Lagrangian (2.1), the last two terms contain three-legged vertices $\propto \delta\sigma F\tilde{F}$ and $\propto h_{ij}\{\dot{A}_i\dot{A}_j + \ldots\}$ that capture the inverse decay of amplified gauge field fluctuations to the spectator scalar and tensor fluctuations, respectively [42,45]. The presence of these vertices ensure correlations between the observable scalar sector $\delta\phi \propto \mathcal{R}$ and the metric h_{ij} perturbations thanks to the mass mixing between $\delta\phi - \delta\sigma$ that we discussed earlier. Therefore, we expect the effects of the particle production processes in the gauge field sector to propagate to the three-point functions of mixed type such as $\langle\hat{\mathcal{R}}\,\hat{h}\,\hat{h}\rangle$[13] and $\langle\hat{h}\,\hat{\mathcal{R}}\,\hat{\mathcal{R}}\rangle$. The diagrams that contribute to these non-Gaussianities can be pictorially represented as in Fig. 2.

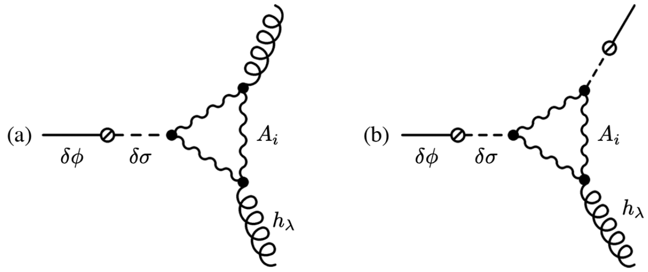

FIG. 2. Diagrammatic representation of the interactions that contribute to the mixed non-Gaussianity of STT-type $\langle\mathcal{R}hh\rangle$ (a) and TSS-type $\langle h\mathcal{R}\mathcal{R}\rangle$ (b) correlators in the rolling spectator axion-gauge field models.

In Appendix D, we calculate both types of mixed non-Gaussianity for the two different rolling axion spectator models [see Eq. (2.6)] that we introduced in the previous section. In the following sections, we present our results and discuss their size and shape dependence.

A. Results for TSS- and STT-type correlators

We are interested in the three-point cross-correlation of comoving curvature perturbation and gravity wave polarization modes, in particular, in the following mixed-type non-Gaussian correlators that are defined by

$$\langle\hat{\mathcal{R}}(0,\vec{k}_1)\hat{h}_\lambda(0,\vec{k}_2)\hat{h}_\lambda(0,\vec{k}_3)\rangle \equiv \mathcal{B}_{\mathcal{R}\lambda\lambda}(\vec{k}_1,\vec{k}_2,\vec{k}_3)\delta(\vec{k}_1+\vec{k}_2+\vec{k}_3),$$
$$\langle\hat{h}_\lambda(0,\vec{k}_1)\hat{\mathcal{R}}(0,\vec{k}_2)\hat{\mathcal{R}}(0,\vec{k}_3)\rangle \equiv \mathcal{B}_{\lambda\mathcal{R}\mathcal{R}}(\vec{k}_1,\vec{k}_2,\vec{k}_3)\delta(\vec{k}_1+\vec{k}_2+\vec{k}_3). \qquad (3.1)$$

As we mentioned in the case of two-point correlators above, mixed-type non-Gaussianities are given by a simple sum of vacuum and sourced contributions: $\mathcal{B}_j = \mathcal{B}_j^{(v)} + \mathcal{B}_j^{(s)}$. In this work, we will disregard the vacuum component of mixed correlators as they are subdominant in the presence of particle production processes involving vector fields.

As in the case of two-point functions, mixed three-point correlators of $\hat{\mathcal{R}}^{(s)}$, $\hat{h}_-^{(s)}$ inherit the scale-dependent amplification of vector fields triggered by the transient motion of the spectator axion $\sigma(t)$. In particular, we found (see Appendix D) that both bispectra can be factorized as

$$\mathcal{B}_j^{(s)}(\vec{k}_1,\vec{k}_2,\vec{k}_3) = \frac{[\epsilon_\phi \mathcal{P}_{\mathcal{R}}^{(v)}]^3}{(k_1k_2k_3)^2} f_j^{(3)}(\xi_*,\delta,x_*,x_2,x_3), \qquad (3.2)$$

where $f_j^{(3)}$ with $j = \{\mathcal{R}\lambda\lambda, \lambda\mathcal{R}\mathcal{R}\}$ are dimensionless functions that parametrize the scale and shape dependence of the bispectrum noting the definitions $x_* = k/k_*$ and $k_1 = k, x_2 = k_2/k_1, x_3 = k_3/k_1$. In the following, we will first focus on the scale dependence of the mixed bispectra to set the stage for a discussion on its amplitude and shape dependence. In our analysis, we found some qualitative differences between TSS- and STT-type mixed three-point correlators, and hence, we will discuss each case separately below.

1. *TSS correlators*

To study the scale dependence of $f_{\lambda\mathcal{R}\mathcal{R}}^{(3)}$, we focus on the equilateral configuration to work out the $x_* = k/k_*$

---

[13] There is an additional four-legged vertex $hhAA$ that appears at the same order as the three-legged vertex hAA (see Fig. 2) in the gravitational coupling $M_{\rm pl}^{-2}$ [64]. Combined with a three-legged scalar vertex $\delta\sigma AA$ and $\delta\phi - \delta\sigma$ mixing, $hhAA$ leads to an additional diagram that contributes to the STT correlator. However, such a diagram contains fewer internal gauge field modes compared to the left diagram in Fig. 2 and thus carry less particle production effects. In particular, counting the number of gauge field modes that contribute to the loop integral [see, e.g., (D8)], we anticipate that the diagram that includes $hhAA$ will be suppressed by a factor of $e^{-2c\pi\xi_*}$ [$c \simeq \mathcal{O}(1)$, see Table III] compared to the diagram we are computing in this work.

TABLE I. The height $f^c_{3,j}$, location $x^c_{3,j}$, and width $\sigma_{3,j}$ of $f^{(3,\alpha)}_{h\mathcal{R}\mathcal{R}}$ (3.3) for $\delta = 0.3$. For the large peak associated ($\alpha = L$) with the $j = -\mathcal{R}\mathcal{R}$ correlator and $j = +\mathcal{R}\mathcal{R}$, the fitting formulas are valid and $3.5 \le \xi_* \le 6.5$, while for the small peak ($\alpha = S$) of the $j = -\mathcal{R}\mathcal{R}$ correlator, they are valid for $4 \le \xi_* \le 5$. The amplitude of the $j = -\mathcal{R}\mathcal{R}$ correlator is positive $f^c_{3,j} > 0$ for the small peak and $f^c_{3,j} < 0$ for the large peak. The $j = +\mathcal{R}\mathcal{R}$ bispectrum has a single peak with a negative amplitude $f^c_{3,j} < 0$.

$\{j\}_\alpha$	$\ln(\lvert f^c_{3,j}\rvert)$	$x^c_{3,j}$	$\sigma_{3,j}$
$\{-\mathcal{R}\mathcal{R}\}_{\mathrm{S,M1}}$	$-20.75 + 17.87\xi_* - 0.109\xi_*^2$	$-2.59 + 1.336\xi_* - 0.0366\xi_*^2$	$0.48 - 0.166\xi_* + 0.0234\xi_*^2$
$\{-\mathcal{R}\mathcal{R}\}_{\mathrm{L,M1}}$	$-8.20 + 14.60\xi_* + 0.121\xi_*^2$	$2.94 + 0.980\xi_* + 0.0294\xi_*^2$	$0.85 - 0.133\xi_* + 0.0076\xi_*^2$
$\{+\mathcal{R}\mathcal{R}\}_{\mathrm{M1}}$	$-10.10 + 14.69\xi_* + 0.119\xi_*^2$	$2.66 + 0.516\xi_* + 0.0195\xi_*^2$	$0.83 - 0.108\xi_* + 0.0065\xi_*^2$
$\{-\mathcal{R}\mathcal{R}\}_{\mathrm{S,M2}}$	$-29.67 + 17.53\xi_* - 0.121\xi_*^2$	$-0.78 + 1.345\xi_* - 0.0295\xi_*^2$	$-0.34 + 0.224\xi_* - 0.0222\xi_*^2$
$\{-\mathcal{R}\mathcal{R}\}_{\mathrm{L,M2}}$	$-20.34 + 14.88\xi_* + 0.0708\xi_*^2$	$7.10 + 0.345\xi_* + 0.0832\xi_*^2$	$0.63 - 0.095\xi_* + 0.0048\xi_*^2$
$\{+\mathcal{R}\mathcal{R}\}_{\mathrm{M2}}$	$-22.84 + 15.17\xi_* + 0.0503\xi_*^2$	$6.03 - 0.128\xi_* + 0.0748\xi_*^2$	$0.69 - 0.100\xi_* + 0.0069\xi_*^2$

dependence of (D9) at fixed values of the background parameters $\{\xi_*, \delta\}$. In the following, we will discuss $-\mathcal{R}\mathcal{R}$- and $\{+\mathcal{R}\mathcal{R}\}$-type correlators separately.

$-\mathcal{R}\mathcal{R}$ *bispectrum.*—Computing (D9) numerically for a grid of $x_* = k/k_*$ values at the equilateral configuration $x_2 = x_3 = 1$, we found that the $-\mathcal{R}\mathcal{R}$ bispectrum can be accurately captured by a sum of two distinctive peaks $f^{(3)}_{-\mathcal{R}\mathcal{R}} = f^{(3,S)}_{-\mathcal{R}\mathcal{R}} + f^{(3,L)}_{-\mathcal{R}\mathcal{R}}$ that have the Gaussian form

$$f^{(3,\alpha)}_j\left(\xi_*, \frac{k}{k_*}, \delta\right) \simeq f^{c,\alpha}_{3,j}[\xi_*, \delta] \exp\left[-\frac{1}{2\sigma^{\alpha}_{3,j}[\xi_*, \delta]^2} \times \ln^2\left(\frac{k}{k_* x^{c,\alpha}_{3,j}[\xi_*, \delta]}\right)\right], \tag{3.3}$$

where we use $\alpha = \{S, L\}$ to label each peak (i.e., a small one and a large one) and $j = -\mathcal{R}\mathcal{R}$. As in the case of two-point correlators we mentioned earlier, the height $f^c_{3,j}$, width $\sigma_{3,j}$, and location $x^c_{3,j}$ of $f^{(3)}_j$'s peak is controlled by the background motion of the spectator axion, namely, by the maximal velocity reaches $\xi_* = -\alpha_c \dot{\sigma}_*/2Hf$ and the total number of e-folds $\dot{\sigma}$ significantly differs from zero during its rollover: $\Delta N \sim \delta^{-1} \sim H^2/m^2_{\mathrm{axion}}$ where m_{axion} is the mass of σ in its global minimum. At a fixed value of ξ_*, increasing δ would generically reduce $f^c_{3,j}$, width $\sigma_{3,j}$, and location $x^c_{3,j}$ because fewer gauge field modes can be amplified to excite cosmological perturbations as $\dot{\sigma}$ will be large for a shorter amount of time in this case. For $\delta = 0.3$, we determined the ξ_* dependence of $f^c_{3,j}$, $\sigma_{3,j}$, and $x^c_{3,j}$ by fitting the right-hand side of Eq. (3.3) to reproduce the position, height, and width of the sourced peaks parametrized by the integral (D9). In Table I, we present the ξ_* dependence of these fitting formulas that appear in (3.3) that approximates the result from the direct numerical integration of (D9). For both models we study in this work, the accuracy of the expression (3.3) is shown in Fig. 3.

A distinctive feature of the $-\mathcal{R}\mathcal{R}$ correlator is its doubly peaked structure which occurs with different signs and locations in k space. In particular, $\langle \hat{h}\_\hat{\mathcal{R}}\hat{\mathcal{R}}\rangle$ exhibits a small positive peak $f^{c,S}_{3,j} > 0$ that occurs slightly earlier in k space ($x^{c,S}_{3,j} < x^{c,L}_{3,j}$) compared to the following large peak realized in the opposite direction ($f^{c,S}_{3,j} < 0$). It is worth mentioning that such a feature is absent in the autocorrelators of sourced curvature $\mathcal{R}$ and h metric perturbations [40,41]. It would be interesting to investigate quantitatively whether

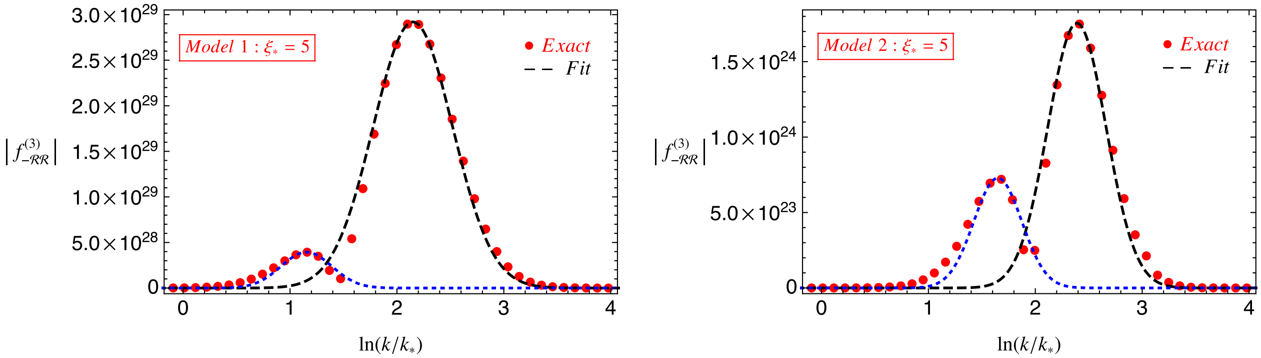

FIG. 3. The scale dependence of total $f^{(3)}_{-\mathcal{R}\mathcal{R}}$ for Model 1 (left) and Model 2 (right). The red points are obtained by direct numerical evaluation of (D9) for a grid of $x_* = k/k_*$ values. Using Table I, we represent the accuracy of the Gaussian expression (3.3) (dashed lines) in parametrizing the large and small peaks that constitute the total signal. Note that the first peak occurs while $f^{(3)}_{-\mathcal{R}\mathcal{R}} > 0$, while for the second peak $f^{(3)}_{-\mathcal{R}\mathcal{R}} < 0$.

the presence of such a small peak increases the observability of the TSS bispectrum. We present an analysis of the double-peak structure of the $-\mathcal{R}\mathcal{R}$ correlator (D9) by comparing it with the $\mathcal{R}--$ (see below) correlator in Appendix D where we show that the reason for this behavior stems from the product of polarization vectors [see, e.g., Eq. (D10)] which serve the purpose of angular momentum conservation at each vertex in the diagrams of Fig. 2. In particular, within the range of loop momenta where the gauge field sources have appreciable contribution to the $-\mathcal{R}\mathcal{R}$ diagram, we found that the product of polarization vectors in (D10) have a sufficiently large negative and positive peak depending on the orientation of the loop momentum (i.e., nonplanar vs planar) with respect to the plane (x-y) where external momenta lives (see Fig. 10). Integrating over such configurations of the loop momentum [see Eq. (D9)] therefore yields a double-peaked structure that occurs in opposite directions as we explain in detail in Appendix D 3. In what follows, in our discussion on the amplitude and shape of the TSS-type bispectrum in Sec. III B, we will focus our attention on the large peak that appears in Fig. 3 which constitutes the dominant scale-dependent signal within the parameter space where $r_s \gg r_{\rm vac}$ (see Fig. 1).

Another conclusion that can be drawn from Table I and Fig. 3 is that Model 2 generically generates signals that have a smaller width compared to Model 1 for the same parameter choice $\delta = 0.3$ ($\sigma_{3,j}^{(\rm M1)} > \sigma_{3,j}^{(\rm M2)}$), which in turn implies that the former requires a larger maximal value for the effective coupling ξ_* between σ and A_μ to generate a signal comparable in amplitude with Model 1.

$+\mathcal{R}\mathcal{R}$ bispectrum.—We found that the $j = +\mathcal{R}\mathcal{R}$ correlator consists of a single peak that has the same Gaussian form as in (3.3). We provide the fitting formulas for this case in the third and sixth rows of Table I. We see that due to the parity violation in the tensor sector, the amplitude of $f^{(3)}_{+\mathcal{R}\mathcal{R}}$ is about an order of magnitude smaller than the $j = -\mathcal{R}\mathcal{R}$ bispectrum. Note that this parity violation is not dramatic because $\langle \hat{h}_\lambda \hat{\mathcal{R}} \hat{\mathcal{R}} \rangle$-type non-Gaussianity contains only a single external state of the tensor perturbation with a definite polarization $\lambda = \pm$. In general, we expect the parity violation in mixed three-point amplitudes to increase for an increasing number of external h_λ in the bispectrum. In fact, as we will show, this is the case for the STT-type bispectrum $\langle \hat{\mathcal{R}} \hat{h}_\lambda \hat{h}_\lambda \rangle$ below (see Sec. III A 2).

2. STT correlator

Repeating the analysis we performed for the TSS-type correlator, we found that the scale dependence of $f^{(3)}_{\mathcal{R}\lambda\lambda}$ in (D8) can instead be described by a single Gaussian peak (see Appendix D 3) that takes the same form as in (3.3). For $3.5 \leq \xi_* \leq 6.5$, its height, width, and location can be well fitted by the second order formulas we provide in Table II, and the accuracy of these formulas compared to the exact numerical computation of (D8) is shown in Fig. 4. From Table II, we see that parity violation presents itself stronger for the STT compared to the TSS bispectrum, as expected since it has a more external tensor mode that carries a definite polarization. On the other hand, $\mathcal{R}h_\lambda h_\lambda$ carries similar features to the TSS correlator; e.g., the width of the signal in Model 1 is larger than the second, which in turn implies that Model 2 requires a larger effective coupling ξ_* to generate the same amount of signal. This situation appears to hold generically for any correlator containing observable fluctuations $\mathcal{X} = \{\mathcal{R}, h_\lambda\}$ and stems from the fact that in the second model (M2), the spectator axion probes a sharper region of its potential (i.e., clifflike regions) compared to Model 1, leading to the excitation of a smaller number of gauge field modes when the particle production is maximal, i.e., around $\tau \sim \tau_*$.

B. Amplitude and shape dependence of mixed non-Gaussianities

Having studied the scale-dependent amplification of non-Gaussian signals of mixed type, in this section we investigate their amplitude and shape.

1. Amplitude of the bispectra

To quantify the size of the mixed non-Gaussianity, we will make use of the standard definition of the nonlinearity parameter evaluated at the equilateral configuration [28,65],

$$f^j_{\rm NL}(k) = \frac{10}{9} \frac{k^6}{(2\pi)^{5/2}} \frac{\mathcal{B}^{(s)}_j(\vec{k}, \vec{k}, \vec{k})}{\mathcal{P}^2_{\mathcal{R}}(k)}, \tag{3.4}$$

where we restrict our analysis to the dominant correlators $j = \{\mathcal{R}--, -\mathcal{R}\mathcal{R}\}$ (see Tables I and II). As we showed in the previous section, the transient particle production in the gauge field sector leads to a scale-dependent bump in the

TABLE II. Fitting formulas for the height $f^c_{3,j}$, location $x^c_{3,j}$, and width $\sigma_{3,j}$ that parametrize the scale-dependent enhancement of the $j = \{\mathcal{R}\lambda\lambda\}$-type mixed bispectrum in (3.2). Formulas are obtained for $\delta = 0.3$ and $3.5 \leq \xi_* \leq 6.5$.

$\{j\}$	$\ln(\lvert f^c_{3,j}\rvert)$	$x^c_{3,j}$	$\sigma_{3,j}$
$\{\mathcal{R}--\}_{\rm M1}$	$-7.21 + 14.77\xi_* + 0.117\xi_*^2$	$3.15 + 0.665\xi_* + 0.0213\xi_*^2$	$0.82 - 0.109\xi_* + 0.0066\xi_*^2$
$\{\mathcal{R}++\}_{\rm M1}$	$-15.6 + 14.74\xi_* + 0.121\xi_*^2$	$1.24 + 0.232\xi_* + 0.0147\xi_*^2$	$0.80 - 0.123\xi_* + 0.0085\xi_*^2$
$\{\mathcal{R}--\}_{\rm M2}$	$-18.9 + 15.15\xi_* + 0.0526\xi_*^2$	$6.60 + 0.050\xi_* + 0.0731\xi_*^2$	$0.65 - 0.089\xi_* + 0.0058\xi_*^2$
$\{\mathcal{R}++\}_{\rm M2}$	$-27.7 + 15.25\xi_* + 0.0484\xi_*^2$	$1.92 + 0.290\xi_* + 0.0083\xi_*^2$	$0.57 - 0.064\xi_* + 0.0034\xi_*^2$

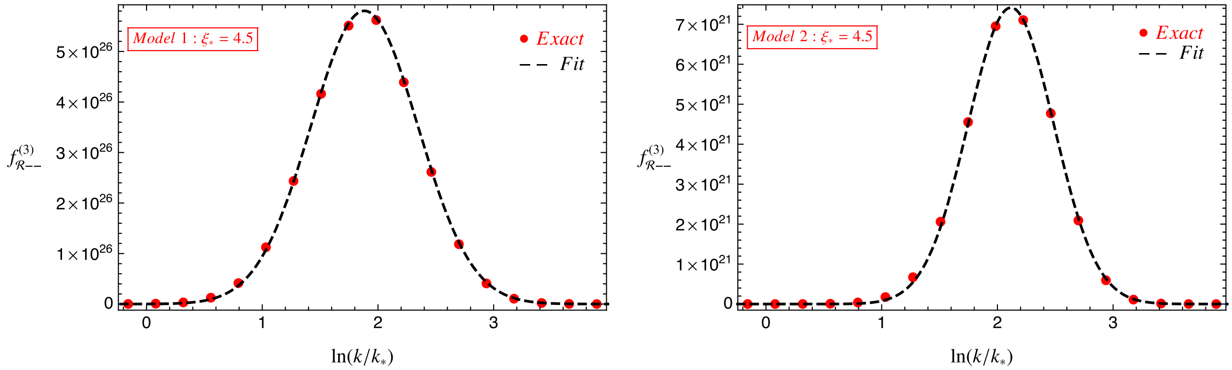

FIG. 4. The scale dependence of $f^{(3)}_{\mathcal{R}--}$ for Model 1 (left) and Model 2 (right) described by the potentials (2.6) in the spectator axion-gauge field model (2.1). The red dots are obtained by numerical evaluation of (D8) at $x_2 = x_3$ for a grid of $x_* = k/k_*$ values, and dashed lines show the accuracy of the Gaussian expression (3.3) where we utilized Table II.

three-point correlators of mixed type. To estimate the maximal size of the nonlinearity parameters $f^j_{\rm NL}$, we therefore use (3.2) to evaluate (3.4) at the peak of the sourced GW signal, $k = k_* x^c_{2,-}$ (see Table IV).

To visualize the relevant parameter space where mixed non-Gaussianity is significant, in Fig. 5, we plot $f^j_{\rm NL} = 10$ curves in the model parameter space $(\epsilon_\phi - \xi_*)$. We see that the parameter space where the GWs sourced by the gauge field sources dominate (on the right-hand side of the $R_t = 1$ line in Fig. 5) overlaps the sizeable values of $f^j_{\rm NL}$. In this regime, $f^j_{\rm NL}$ can be parametrized in terms of the peak value of the tensor-to-scalar ratio r_p (B3) as

$$f^{\mathcal{R}--}_{\rm NL} \simeq \begin{cases} 24\left(\frac{r_p}{0.01}\right)^{3/2} e^{0.025\xi_*} & (\text{Model}\,1), \\ 11\left(\frac{r_p}{0.01}\right)^{3/2} e^{0.082\xi_*} & (\text{Model}\,2) \end{cases} \tag{3.5}$$

and

$$f^{-\mathcal{R}\mathcal{R}}_{\rm NL} \simeq \begin{cases} 8\left(\frac{r_p}{0.01}\right)^{3/2} e^{-0.099\xi_*} & (\text{Model}\,1), \\ 1.6\left(\frac{r_p}{0.01}\right)^{3/2} e^{-0.009\xi_*} & (\text{Model}\,2), \end{cases} \tag{3.6}$$

where the ξ_* dependence is weak and hence can be ignored for the parameter space of interest $3.5 \le \xi_* \le 6.5$. The origin of $f^j_{\rm NL} \propto r_p^{3/2}$ scaling for the STT and TSS correlators can be understood as follows. In the effective particle production regime we are interested in $(R_t > 1)$, the tensor power spectrum arises through a loop diagram that contains two copies of the three-legged vertex in Fig. 2, i.e., $(hAA)^2 \propto A^6$, and thus carries a weight factor of $(e^{c\pi\xi_*})^4$ (see Table III) that characterizes the amplification of gauge modes by the transiently rolling spectator axion. Therefore, evaluated at the peak of scale-dependent signals, the one loop diagram involving two external gravitons gives $\mathcal{P}_h \propto r_p \propto e^{4c\pi\xi_*}$ for $R_s < 1$. On the other hand, we notice from Fig. 2 that the diagrams that contribute to the TSS and STT correlators originate from the fusion of three-point tensor and scalar vertices of the form $(hAA)^2 \times ([\delta\phi \leftarrow \delta\sigma]AA)$ and $(hAA) \times ([\delta\phi \leftarrow \delta\sigma]AA)^2$, and thus, we roughly have

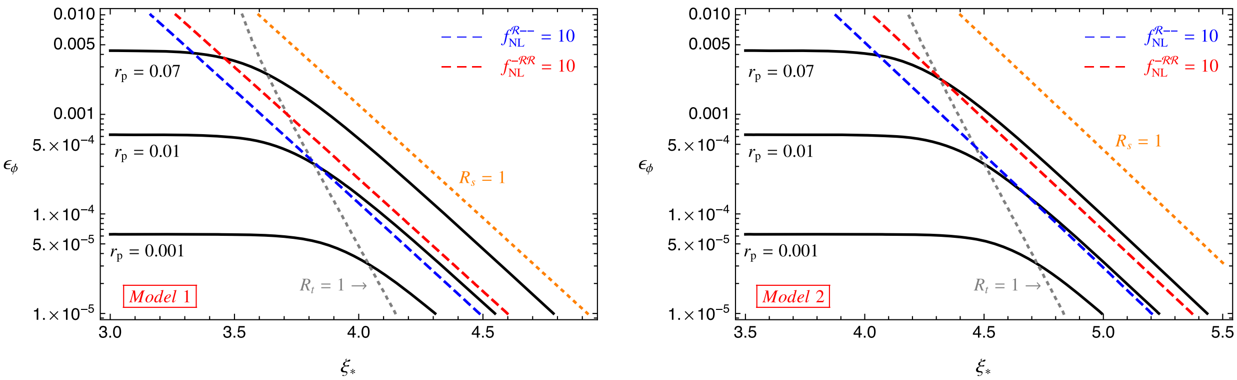

FIG. 5. Constant $f^j_{\rm NL}$ curves superimposed with constant r curves in the $\epsilon_\phi - \xi_*$ plane for Model 1 (left) and Model 2 (right). The color coding and the parameter choices are the same as in Fig. 1.

$f^{j}_{\rm NL} \propto \mathcal{B}^{j} \propto A^{6} \propto e^{6c\pi\xi_*}$ for $R_s < 1$. Putting together the arguments above thus gives the scaling $f^{j}_{\rm NL} \propto r_p^{3/2}$.

At this point, it is useful to compare these results with the TSS- and STT-type non-Gaussianity obtained in single-field inflation where $f^{\mathcal{R}--}_{\rm NL} \sim r^2$ and $f^{-\mathcal{R}\mathcal{R}}_{\rm NL} \sim r$ is expected [66]. In this respect, the results in (3.5) and (3.6) can be considered as a new set of consistency conditions that can be utilized to distinguish particle production scenarios involving Abelian gauge fields from the conventional ones. In particular, these results indicate that the gauge field production induced by the rolling axions can clearly alter the parametric dependence of nonlinearity parameters on r, and STT and TSS mixed non-Gaussianity shows a significant enhancement with respect to the standard results from single-field inflation. Furthermore, the relative locations of the $f^{-\mathcal{R}\mathcal{R}}_{\rm NL}$ and $f^{\mathcal{R}--}_{\rm NL}$ curves in Fig. 5 indicated that the non-Gaussianity associated with the latter is larger for a given ξ_* that parametrizes the strength of gauge field production. On the other hand, a comparison between Tables I and II reveals that the level of parity violation is more emphasized for the STT bispectrum compared to TSS. As we mentioned above, this result is expected since the STT-type correlator contains a more external tensor mode with a definite parity $\lambda = \pm$.

2. *Shape of the mixed bispectra*

We now turn our attention to the shape of the mixed non-Gaussianity. For this purpose, it is customary to extract the overall k^{-6} scaling of the bispectrum in (3.2) by defining the shape function S_j as [67,68]

$$S_j(k_1,k_2,k_3) = \mathcal{N}(k_1k_2k_3)^2\mathcal{B}^{(s)}_j(\vec{k}_1,\vec{k}_2,\vec{k}_3) \propto f^{(3)}_j(\xi_*,x_*,\delta,x_2,x_3), \tag{3.7}$$

where $\mathcal{N}$ is an arbitrary normalization factor. We pick a normalization factor $\mathcal{N}$ to ensure $S_j = 1$ at the triangle configuration $f^{(3)}_j$ becomes maximal (obtained numerically). Then, focusing on isosceles triangles $k_2 = k_3$ ($x_2 = x_3$), we evaluate the shape function on a grid of values in the $k_1/k_* - k_2/k_*$ plane for $j = \{\mathcal{R}--, -\mathcal{R}\mathcal{R}\}$ and plot the resulting constant contour lines corresponding to $S_j = \{0.9, 0.7, 0.5, 0.3\}$ values of the shape function in Fig. 6. We note that, due to the triangle inequality $k_2 + k_3 \geq k_1$, only triangle configurations that satisfy $k_1 \leq 2k_2$ ($x_2 \geq 1/2$) are allowed, as shown by the limiting blue dashed lines shown in Fig. 6.

We observe from the shape of the contour lines (such as their spread in the $k_1 - k_2$ plane and the approximate locations of the maximum) that both of the rolling axion models lead to a qualitatively similar result for each type of mixed bispectrum. A slightly different behavior appears for the TSS correlator in the rolling axion monodromy model (M2) where the spread of the contour lines take up a smaller area in the $k_1 - k_2$ plane. The reason for this is the fact that for the same parameter choices, the second model contains a sharper feature in its dynamics compared to M1. In particular, the physical quantity that controls the gauge field production, i.e., the velocity of $\dot{\sigma}$, has a more spiky behavior in the second model, leading to the excitation of a smaller range of gauge field modes that can in turn source tensor and scalar fluctuations. This effect becomes more emphasized as the number of external $\mathcal{R}$ in the three-point function increases because the sourced curvature perturbation is more susceptible to the background evolution of the rolling axion, as can be verified explicitly by comparing Eqs. (A6)–(A9). The similarity of the shapes of the contour lines in the STT correlators (top row) in Fig. 6 also supports these arguments.

As indicated by the location of the black dots in Fig. 6, a common feature of the mixed correlators is that they are maximized for triangle configurations close to the equilateral shape. In particular, away from the maximum, the shape function reduces considerably in magnitude toward the folded $k_1/k_* \to 2k_2/k_*$ and squeezed configurations $k_1/k_* \to 0$, implying that the shape of the STT and TSS bispectra are distinct from such configurations. Besides the general features we covered so far, there are some quantitative differences in the properties of the shape functions which we discuss in detail below.

(i) STT: From the top panel in Fig. 6, notice that mixed correlators are maximal at scales that slightly deviate from the exact equilateral configuration; i.e., $S_{\mathcal{R}--} = 1$ (black dots) at $k_2 > k_1$ for both models.
   This slight deviation from the exact equilateral configuration is closely tied to the offset that appears in the locations of the sourced curvature perturbation $\mathcal{R}$ and h_-. In particular, a close inspection of the peak location of the two-point correlators (see Table IV) reveals $x^c_{2,\mathcal{R}} < x^c_{2,-}$ and naturally leads to the expectation that the peak location of the external momenta (k_1) associated with $\mathcal{R}$ will satisfy $k_1 < k_2$ in the STT correlator.

(ii) TSS: From the bottom panels of Fig. 6, we notice that the TSS bispectrum also takes its maximal value for triangles satisfying $k_2 > k_1$. Considering the discussion we presented above for the STT correlator, this result contradicts with the expectation that the maximum of the TSS bispectra should appear below the equilateral line $k_2 < k_1$ in Fig. 6. We speculate that this peculiarity stems from the products of helicity vectors $\epsilon_{(-\mathcal{R}\mathcal{R})}$ [defined in (D10)] that appear inside the integral (D9) of $f^{(3)}_{-\mathcal{R}\mathcal{R}}$ that characterize the shape function $S_{-\mathcal{R}\mathcal{R}} \propto f^{(3)}_{-\mathcal{R}\mathcal{R}}$, which should have more support for $x_2 > 1$ ($k_2 > k_1$).

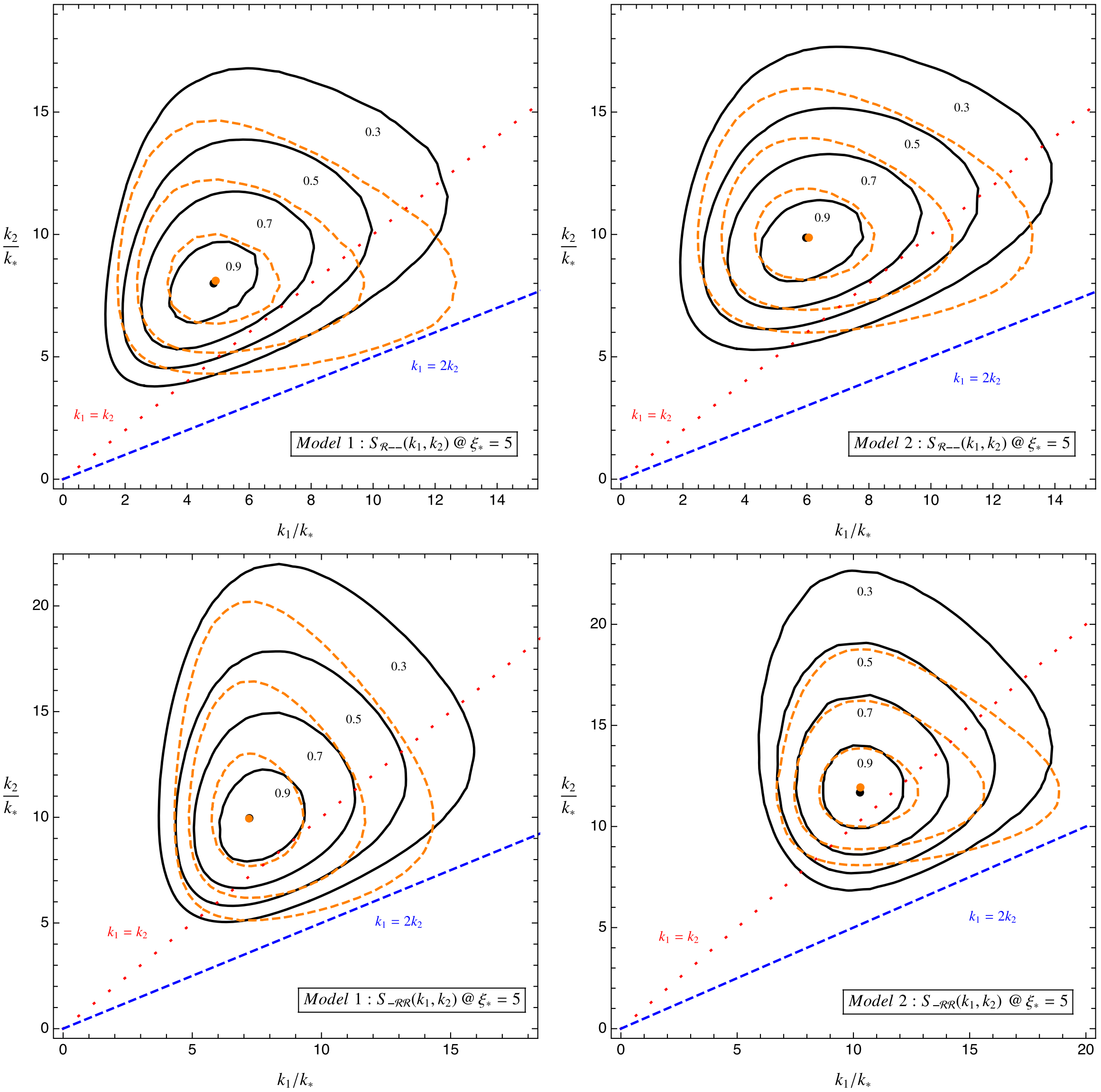

FIG. 6. Constant contour lines of the shape $S_{\mathcal{R}--}$ (top panel) and $S_{-\mathcal{R}\mathcal{R}}$ (bottom panel) in the $k_1/k_* - k_2/k_*$ plane, respectively, for the TSS and STT mixed bispectrum and for both rolling axion models we consider in this work. The black dots locate the triangle configuration for which the bispectrum is maximum ($S_j = 1$). Orange dashed lines indicate the $S_j = 0.9, 0.7, 0.5$ contour lines derived from the approximate expressions (E1) (top) and (E2) (bottom), while the orange dot locates the triangle configuration of their corresponding maximum. The red dotted line and the blue dashed line refer to equilateral triangles $k_1 = k_2$ and folded triangles $k_1 = 2k_2$, respectively.

To speed up its analysis with the actual data, in Appendix E, we derive approximate expressions for the mixed bispectra written as a sum of factorized terms. In particular, we provide approximate expressions for the bispectra such that each term in these expressions [see, e.g., (E1) and (E2)] is written as a product of source functions $f_{2,j}$ and $f_j^{(3)}$ that depend on only one external momenta, k_i. In Fig. 6, we illustrate the accuracy of these approximate expressions by the orange dashed lines and orange dots corresponding to $S_j = 0.9, 0.7, 0.5$ contour lines and the $S_j = 1$ point, respectively. As shown in the figure, we observe that the maxima derived from the approximate formulas (orange dots) are nearly coincident with the actual ones (black dots), and the approximate expressions provide an accurate description of the exact bispectra, particularly around the maximum.

IV. CONCLUSIONS

In this work, we focused our attention on a class of inflationary scenarios characterized by a system (2.1) of spectator axion and U(1) gauge fields coupled by a Chern-Simons-type interaction [40,41]. In these models, the transient roll of the spectator axion triggers a localized enhancement in the gauge field fluctuations, which in turn induces several phenomenologically interesting signatures in the CMB observables, including a low energy scale realization of inflation endowed with a scale-dependent chiral GW signal accessible by forthcoming observations [40] together with observable tensor non-Gaussianity [51]. While bounds on the scalar two-point and three-point autocorrelators from the CMB observables can be avoided for the parameter space that leads to interesting phenomenology in the tensor sector, the spectator axion-U(1) gauge field dynamics also predict enhanced scalar fluctuations by the gauge fields. Therefore in this setup, mixed non-Gaussianities including scalar and tensor fluctuations appear to be as important as the information one can gain from their autocorrelators. In particular, the nontrivial parity violating structure of these correlators may provide additional predictive power, help us constrain the model parameters, and reveal distinguishing features that can provide effective model comparison, e.g., considering the absence/presence of the analog signals that are present within the standard single-field inflation or the close SU(2) cousin [69,70] of the model we consider in this work.

To shed some light on these issues, we derived predictions for the scalar-tensor-tensor and tensor-scalar-scalar bispectrum focusing on spectator axion-U(1) gauge field dynamics during inflation (see Sec. III). We find that both bispectra exhibit a scale-dependent amplification, and at the their respective peaks, they are significantly enhanced compared to their counterparts in the minimal single-field inflationary scenario [see, e.g., Eqs. (3.5) and (3.6)]. In particular, in the efficient particle production regime, we found that mixed non-Gaussian correlators satisfy a new consistency condition $f^{j}_{\rm NL} \simeq \mathcal{O}(1-10)(r/0.01)^{3/2}$ that distinguishes these models from the conventional single-field scenarios. More importantly, due to the parity violating nature of gauge field production, the resulting mixed bispectra also exhibit a preferred chirality. In Sec. III B, we studied the shape dependence of these amplified signals and found that both bispectra are maximal *close* to the equilateral shape, slightly deviating from the exact equilateral configuration (see Fig. 6). Given that the sources (gauge fields) of these correlators have maximal amplitudes at around the horizon crossing (see Table IV), this result is expected.

The detectability of the scale-dependent parity violating $\langle \hat{\mathcal{R}}\hat{h}_\lambda\hat{h}_\lambda\rangle$ and $\langle \hat{h}_\lambda\hat{\mathcal{R}}\hat{\mathcal{R}}\rangle$ signals we studied in this work require a detailed analysis of the CMB observables. A possibility in this direction would be to consider cross-correlations between the CMB temperature T and E,B polarization modes. In particular, to search for a primordial STT bispectrum, a suitable observable would be TBB and EBB cross-correlations of the CMB (see, e.g., [55,71,72]), whereas the observability of the TSS bispectrum can be analyzed through BTT or BEE (see, e.g., [73]). In this respect, the approximate factorized expressions we derived for both bispectra (see Appendix E) can be utilized to test mixed non-Gaussian signals of the rolling spectator axion models. On the other hand, although we focused much of our attention on the impact of scalar and tensor cross-correlations at CMB scales in this work, rolling spectator axion models can also produce interesting signals at much smaller cosmological scales (see, e.g., [34,41]). In this context, it would be interesting to explore observables that parity violating STT and TSS correlators may induce at sub-CMB scales. We leave further investigations of these issues for a future publication.

ACKNOWLEDGMENTS

We would like to thank Marco Peloso, Maresuke Shiraishi, and Caner Ünal for comments and useful discussions pertaining this work. Part of this research project was conducted using computational resources at the Physics Institute of the Czech Academy of Sciences, and we acknowledge the help of Josef Dvoracek with this process. This work is supported by the European Structural and Investment Funds and the Czech Ministry of Education, Youth and Sports (Project No. CoGraDS-CZ.02.1.01/0.0/0.0/15003/0000437).

APPENDIX A: GAUGE FIELD MODES AS SOURCES OF SCALAR AND TENSOR PERTURBATIONS

We now summarize some important aspects of the gauge field production and their subsequent sourcing of cosmological perturbations. Considering the time-dependent profile (2.7) of the effective coupling ξ_*, Eq. (2.2) describes the standard Schrödinger equation of the "wave function" A_- for which an analytic solution can be derived by employing WKB approximation methods [40]. In particular, the late-time growing solution to Eq. (2.2) can be parametrized in terms of a scale-dependent normalization (real and positive) factor as [40,41]

$$A_-(\tau,k) \simeq \frac{N_A(\xi_*,-k\tau_*,\delta)}{\sqrt{2k}}\left[\frac{-k\tau}{2\xi(\tau)}\right]^{1/4}\exp\left[-E(\tau)\sqrt{-2\xi_* k\tau}\right],\qquad \tau/\tau_* < 1, \tag{A1}$$

where the time-dependent argument of the exponential factor depends on the model as

$$E(\tau) = \begin{cases} \frac{2\sqrt{2}}{(1+\delta)(\tau/\tau_*)^{-\delta/2}}, & \text{Model 1(M1)}, \\ \frac{2}{\delta|\ln(\tau/\tau_*)|}, & \text{Model 2(M2)}. \end{cases} \tag{A2}$$

The scale dependence ($x_* = k/k_*$) of the normalization factor $N_A(\xi_*, x_*, \delta)$ in (A1) can be determined by solving (2.2) numerically for different values of $x_* = -k\tau_*$ and matching it to the WKB solution (A1) at late

TABLE III. ξ_* dependence of the functions N_A^c, location q_A^c, and width σ_A that appear in the late-time amplitude N_A [Eq. (A3)] of the gauge field modes for $\delta = 0.3$ and $3 \leq \xi_* \leq 6.5$.

	$\ln(N_A^c)$	q_A^c	σ_A
M1	$0.290 + 2.83\xi_* + 0.00100\xi_*^2$	$-0.097 + 0.633\xi_* - 0.00110\xi_*^2$	$2.11 - 0.321\xi_* + 0.0208\xi_*^2$
M2	$0.325 + 2.72\xi_* - 0.00069\xi_*^2$	$0.013 + 0.710\xi_* - 0.00105\xi_*^2$	$1.69 - 0.254\xi_* + 0.0164\xi_*^2$

times $-k\tau \ll 1$. In this way, one can confirm that $N_A(\xi_*, x_*, \delta)$ can be accurately described by a log-normal distribution,

$$N_A(\xi_*, x_*, \delta) \simeq N_A^c[\xi_*, \delta] \exp\left(-\frac{1}{2\sigma_A^2[\xi_*, \delta]} \ln^2\left(\frac{x_*}{q_A^c[\xi_*, \delta]}\right)\right), \tag{A3}$$

where the functions N_A^c, q_A^c, and σ_A parametrize the background dependence of gauge field production, and hence depend on ξ_* and δ. For an effective coupling to gauge fields within the range $3 \leq \xi_* \leq 6.5$, these functions can be described accurately by a second order polynomial in ξ_* provided in Table III. Since the growing solution to the mode functions A_- is real, its Fourier decomposition can be simplified as

$$\hat{A}_i(\tau, \vec{x}) \simeq \int \frac{\mathrm{d}^3 k}{(2\pi)^{3/2}} e^{i\vec{k}.\vec{x}} \epsilon_i^-(\vec{k}) A_-(\tau, \vec{k}) [\hat{a}_-(\vec{k}) + \hat{a}_-^\dagger(-\vec{k})], \tag{A4}$$

where the helicity vectors obey $k_i \epsilon_i^\pm = 0$, $\epsilon_{ijk} k_j \epsilon_k^\pm = \mp ik\epsilon_i^\pm$, $\epsilon_i^\pm \epsilon_i^\pm = 0$, $\epsilon_i^\pm \epsilon_i^\mp = 1$, and $(\epsilon_i^\lambda(\vec{k}))^* = \epsilon_i^\lambda(-\vec{k}) = \epsilon_i^{-\lambda}(\vec{k})$, and the annihilation/creation operators satisfy $[\hat{a}_\lambda(\vec{k}), \hat{a}_{\lambda'}^\dagger(\vec{k}')] = \delta_{\lambda\lambda'} \delta(\vec{k} - \vec{k}')$. Using the definitions of "electric" and "magnetic" from the main text [see below Eq. (2.3)], we obtain their Fourier modes as

$$\begin{aligned} \hat{E}_i(\tau, \vec{k}) &= -\sqrt{\frac{k}{2}} \frac{\epsilon_i^-(\vec{k})}{a(\tau)^2} \left(\frac{2\xi(\tau)}{-k\tau}\right)^{1/4} N_A(\xi_*, -k\tau_*, \delta) \exp\left[-E(\tau)\sqrt{-2\xi_* k\tau}\right] \hat{\mathcal{O}}_-(\vec{k}), \\ \hat{B}_i(\tau, \vec{k}) &= -\sqrt{\frac{k}{2}} \frac{\epsilon_i^-(\vec{k})}{a(\tau)^2} \left(\frac{-k\tau}{2\xi(\tau)}\right)^{1/4} N_A(\xi_*, -k\tau_*, \delta) \exp\left[-E(\tau)\sqrt{-2\xi_* k\tau}\right] \hat{\mathcal{O}}_-(\vec{k}), \end{aligned} \tag{A5}$$

where we defined the following shorthand notation for the superposition of gauge field annihilation and creation operators: $\hat{\mathcal{O}}_\lambda(\vec{q}) \equiv [\hat{a}_\lambda(\vec{q}) + \hat{a}_\lambda^\dagger(-\vec{q})]$.

Electric and magnetic fields defined in (A5) act as sources to cosmological scalar and tensor perturbations. The main channel of contribution to curvature perturbation in this model is schematically given by $\delta A + \delta A \to \delta\sigma \to \delta\phi \propto \mathcal{R}$ [44,45] and can be expressed as [40,41]

$$\hat{\mathcal{R}}^{(s)}(\tau, \vec{k}) \simeq \frac{3\sqrt{2}H\tau}{M_{\mathrm{pl}}} \int d\tau' G_k(\tau, \tau') \times \frac{\sqrt{\epsilon_\sigma(\tau')}}{\tau'^2} \int d\tau'' G_k(\tau', \tau'') \hat{J}_\sigma(\tau'', \vec{k}), \tag{A6}$$

where G_k is the Green's function for the operator $\partial_\tau^2 + k^2 - 2/\tau^2$, and the source term $\hat{J}_\sigma$ is given by

$$\hat{J}_\sigma(\tau'', \vec{k}) = \frac{\alpha_c a(\tau'')^3}{f} \int \frac{\mathrm{d}^3 p}{(2\pi)^{3/2}} \hat{E}_i(\tau'', \vec{k} - \vec{p}) \hat{B}_i(\tau'', \vec{p}). \tag{A7}$$

On the other hand, metric fluctuations are inevitably sourced by the traceless transverse part of the anisotropic energy-momentum tensor as

$$\hat{h}_\lambda^{(s)}(\tau, k) = \frac{2}{a(\tau) M_{\mathrm{pl}}} \int_{-\infty}^{\tau} \mathrm{d}\tau' G_k(\tau, \tau') \hat{J}_\lambda(\tau', \vec{k}), \tag{A8}$$

where J_λ can be expressed as a bilinear convolution of electric and magnetic fields

$$\hat{J}_\lambda(\tau, \vec{k}) = -\frac{a^3(\tau)}{M_{\mathrm{pl}}} \Pi_{ij,\lambda}(\vec{k}) \int \frac{\mathrm{d}^3 p}{(2\pi)^{3/2}} [\hat{E}_i(\tau, \vec{k} - \vec{p}) \hat{E}_j(\tau, \vec{p}) + \hat{B}_i(\tau, \vec{k} - \vec{p}) \hat{B}_j(\tau, \vec{p})], \tag{A9}$$

with $\Pi_{ij,\pm} = \epsilon_i^\mp(\vec{k}) \epsilon_j^\mp(\vec{k})$ the transverse traceless projector with the properties listed below (2.3).

APPENDIX B: FITTING FORMULAS FOR $f_{2,j}$ AND THE TENSOR-TO-SCALAR RATIO

Here we provide some details regarding the two-point power spectra in the rolling spectator axion-gauge field model. Using the definition (2.11) of the tensor-to-scalar ratio with Eqs. (2.9) and (2.10), the full expression for r can be written as

TABLE IV. Fitting formulas for the height $f^c_{2,j}$, location $x^c_{2,j}$, and width $\sigma_{2,j}$ of the peak of the scale-dependent enhancement functions $f_{2,j}$ in (2.10) for $\delta = 0.3$ and $3 \leq \xi_* \leq 6.5$ in Model 1 (top) and Model 2 (bottom).

$\{i,j\}_\alpha$	$\ln(f^c_{i,j})$	$x^c_{i,j}$	$\sigma_{i,j}$
$\{2,\mathcal{R}\}_{\rm M1}$	$-5.97 + 9.69\xi_* + 0.0895\xi_*^2$	$2.30 + 0.518\xi_* + 0.0117\xi_*^2$	$1.10 - 0.134\xi_* + 0.0087\xi_*^2$
$\{2,-\}_{\rm M1}$	$-7.50 + 9.69\xi_* + 0.0920\xi_*^2$	$3.84 + 0.652\xi_* + 0.0291\xi_*^2$	$1.06 - 0.147\xi_* + 0.0094\xi_*^2$
$\{2,\mathcal{R}\}_{\rm M2}$	$-15.13 + 10.09\xi_* + 0.0389\xi_*^2$	$6.63 - 0.403\xi_* + 0.0856\xi_*^2$	$0.89 - 0.101\xi_* + 0.0066\xi_*^2$
$\{2,-\}_{\rm M2}$	$-14.78 + 9.91\xi_* + 0.0487\xi_*^2$	$7.78 - 0.166\xi_* + 0.0992\xi_*^2$	$0.83 - 0.110\xi_* + 0.0070\xi_*^2$

$$r(k) \simeq 16\epsilon_\phi \left[\frac{1 + \frac{\epsilon_\phi}{16}\mathcal{P}^{(v)}_{\mathcal{R}}(k) f_{2,-}(\xi_*, \frac{k}{k_*}, \delta)}{1 + \epsilon_\phi^2 \mathcal{P}^{(v)}_{\mathcal{R}}(k) f_{2,\mathcal{R}}(\xi_*, \frac{k}{k_*}, \delta)}\right], \tag{B1}$$

where $\sum_\lambda \mathcal{P}^{(v)}_\lambda \equiv \mathcal{P}^{(v)}_h = 16\epsilon_\phi \mathcal{P}^{(v)}_{\mathcal{R}}$ is the total tensor vacuum power spectrum, and we have neglected the subdominant positive helicity mode of sourced fluctuations $f_{2,+} \ll f_{2,-}$. In the parametrization provided in (B1), the second terms in the numerator and denominator give the ratio between the sourced and vacuum power spectrum for tensor/scalar fluctuations, respectively,

$$R_t \equiv \frac{\epsilon_\phi}{16}\mathcal{P}^{(v)}_{\mathcal{R}}(k) f_{2,-}\left(\xi_*, \frac{k}{k_*}, \delta\right),$$
$$R_s \equiv \epsilon_\phi^2 \mathcal{P}^{(v)}_{\mathcal{R}}(k) f_{2,\mathcal{R}}\left(\xi_*, \frac{k}{k_*}, \delta\right). \tag{B2}$$

To evaluate the expressions (B1) and (B2), in Table IV, we provide fitting formulas for the height, width, and the position of the peak of $f_{2,j}$ in (2.10) using the exact expressions of these functions that appeared in the Appendixes of [40,41]. We can then use the fitting formulas in Table IV to evaluate the tensor-to-scalar ratio (B1) and the ratios of the sourced to vacuum power spectra in (B2) at the peak scale of the GW signal $k = k_* x^c_{2,-}$. The constant r curves, together with the various R_t and R_s obtained in this way, are shown in the $\epsilon_\phi - \xi_*$ plane in Fig. 1. When the sourced contribution dominates $R_t \gg 1$, we found that tensor-to-scalar ratio (B1) evaluated at its peak $k = k_p = k_* x^c_{2,-}$ can be well approximated by the formula

$$r_p \simeq \epsilon_\phi^2 \begin{cases} e^{10.61(\xi_* - 2.81)} & (\text{Model 1}), \\ e^{10.40(\xi_* - 3.46)} & (\text{Model 2}), \end{cases} \tag{B3}$$

where we linearized the exponent of $(\ln(f^c_{2,-}))$ in Table IV within the range $3.5 \leq \xi_* \leq 6.5$.

APPENDIX C: SHAPE ANALYSIS OF SSS AND TTT CORRELATORS

In this Appendix, we study shape of the scalar and tensor autobispectrum in the noncompact axion monodromy model we described in the main text [see, e.g., (2.6)]. Similar to the mixed non-Gaussianity, the bispectrum can be factorized as [41]

$$\mathcal{B}^{(s)}_j(\vec{k}_1, \vec{k}_2, \vec{k}_3) = \frac{[\epsilon_\phi \mathcal{P}^{(v)}_{\mathcal{R}}]^3}{(k_1 k_2 k_3)^2} f^{(3)}_j(\xi_*, \delta, x_*, x_2, x_3), \tag{C1}$$

where $j = \{\mathcal{RRR}, ---\}$ and $k_1 = k, x_2 = k_2/k$, $x_3 = k_3/k$. To analyze the shape, we use the definition of the shape function (3.7) and utilize the explicit formulas derived in Appendixes B and C of [41] [see, e.g., Eqs. (B.19) and (C.15) in [41]]. We then focus on isosceles triangles $x_2 = x_3$ to numerically evaluate these exact expressions on a grid of values in the k_1/k_* vs k_2/k_* plane and plot in Fig. 7 the constant contour lines (black solid lines) of S_j that correspond to 0.9,0.7,0.5,0.3 of its maximal value (black dots) where $S_j(k_1, k_2) = 1$. We see that similar to Model 1 studied in [40], both bispectra are maximal on an equilateral triangle of scales $k_1 \simeq k_2 = k_3 \simeq \mathcal{O}(5 - 10)k_*$ that is approximately equal to the scales at which the power spectra have a peak (see Table IV). Motivated by this and the invariance of autobispectra under the exchange of any pair of external momenta, an approximate factorized form for the shape function $S \propto f^{(3)}_j$ is postulated in [40]

$$f^{(3)}_j(k_1, k_2, k_3) \simeq \left[\frac{f^{(3)}_j(k_1, k_1, k_1)}{3 f_{2,j}(k_1)^{3/2}} + \frac{f^{(3)}_j(k_2, k_2, k_2)}{3 f_{2,j}(k_2)^{3/2}} + \frac{f^{(3)}_j(k_3, k_3, k_3)}{3 f_{2,j}(k_3)^{3/2}}\right] \prod_{i=1}^{3} f_{2,j}(k_i)^{1/2}, \tag{C2}$$

where we omit the dependence of the sourced quantities $f_{2,j}$ and $f^{(3)}_j$ on ξ_*, δ, and k_* for the simplicity of the notation. The accuracy of (C2) in capturing the actual shape of the bispectra is shown in Fig. 7.

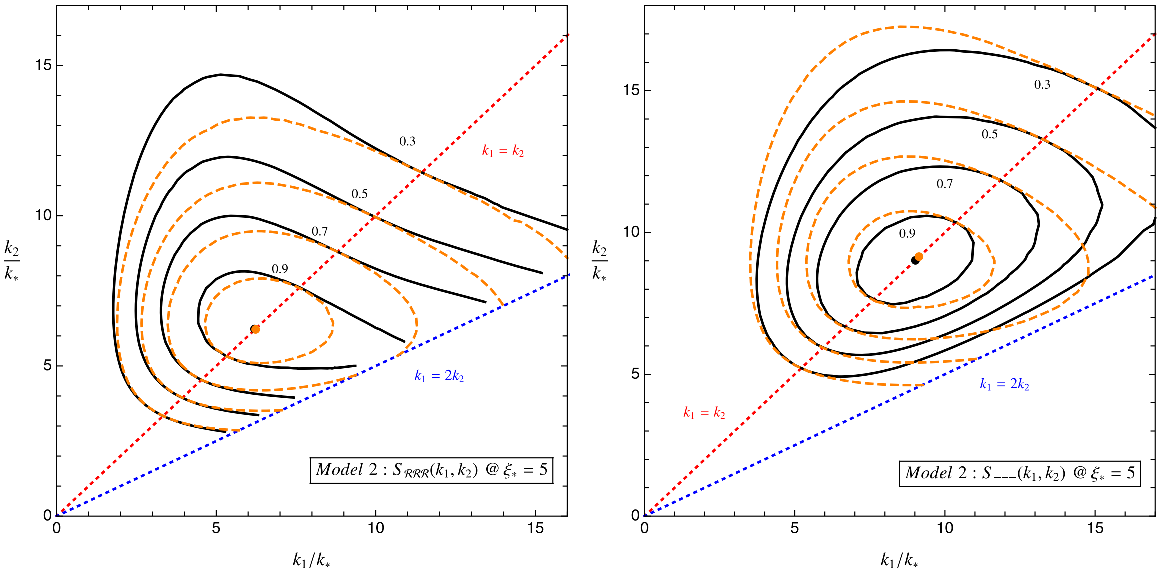

FIG. 7. Constant contour lines of the shape functions $S_{\mathcal{RRR}}$ and S_{---}, respectively, of the $\langle\hat{\mathcal{R}}\hat{\mathcal{R}}\hat{\mathcal{R}}\rangle$ and $\langle\hat{h}_-\hat{h}_-\hat{h}_-\rangle$ bispectra in (3.7) in the noncompact axion model (M2) for an isosceles triangle $k_2 = k_3$ and for $\{\xi_* = 5, \delta = 0.3\}$. The black dots locate the triangle configuration at which the bispectrum is maximum, whereas the orange dot represents the location of the maximum obtained from the approximate expression (C2). The dotted lines are drawn for reference to equilateral triangles $k_1 = k_2$ and folded triangles $k_1 = 2k_2$.

APPENDIX D: COMPUTATIONS OF THE MIXED BISPECTRA

We present here our derivation of the STT and TSS bispectrum. For this purpose, we first note Eq. (A6) and the definitions of electric and magnetic fields in (A5) to write $\mathcal{R}$ as [40,41]

$$\begin{aligned}\hat{\mathcal{R}}^{(s)}(0,\vec{k}) = {} & \left(\frac{H}{M_{\rm pl}}\right)^2 \frac{3\sqrt{2\pi^3}\xi_*}{8k^4}\int \frac{\mathrm{d}^3 p}{(2\pi)^{3/2}}\epsilon_i^-(\vec{k}-\vec{p})\epsilon_i^-(\vec{p})p^{1/4}|\vec{k}-\vec{p}|^{1/4}(p^{1/2}+|\vec{k}-\vec{p}|^{1/2}) \\ & \times N_A(\xi_*,-|\vec{k}-\vec{p}|\tau_*,\delta)N_A(\xi_*,-p\tau_*,\delta)\hat{\mathcal{O}}_-(\vec{k}-\vec{p})\hat{\mathcal{O}}_-(\vec{p})\mathcal{I}_{\mathcal{R}}\left[\xi_*,x_*,\delta,\sqrt{\frac{|\vec{k}-\vec{p}|}{k}}+\sqrt{\frac{p}{k}}\right].\end{aligned} \tag{D1}$$

In (D1), $\mathcal{I}_{\mathcal{R}}$ includes a time integration over the gauge field mode functions [40,41],

$$\mathcal{I}_{\mathcal{R}}[\xi_*,x_*,\delta,Q] \equiv \int_0^\infty \frac{dx'}{x'}J_{3/2}(x')\sqrt{\frac{\epsilon_\sigma(x')}{\epsilon_{\sigma,*}}}\int_{x'}^\infty dx'' x''^{3/2}\exp[-E(x'')\sqrt{2\xi_* x''}Q][J_{3/2}(x')Y_{3/2}(x'')-Y_{3/2}(x')J_{3/2}(x'')], \tag{D2}$$

where $\sqrt{\epsilon_\sigma(x')/\epsilon_{\sigma,*}} = (1+\ln[(x_*/x')^\delta]^2)^{-1}$.

Similarly, plugging the definitions (A5) in (A8) and noting (A9), $\hat{h}_\lambda^{(s)}$ is given by [40,41]

$$\begin{aligned}\hat{h}_\lambda^{(s)}(0,k) \simeq {} & \sqrt{\frac{2}{k^7}}\left(\frac{H}{M_{\rm pl}}\right)^2\int \frac{\mathrm{d}^3 p}{(2\pi)^{3/2}}\epsilon_\lambda[\vec{k},\vec{k}-\vec{p},\vec{p}]p^{1/4}|\vec{k}-\vec{p}|^{1/4}N_A(\xi_*,-|\vec{k}-\vec{p}|\tau_*,\delta) \\ & \times N_A(\xi_*,-p\tau_*,\delta)\mathcal{I}_h\left[\xi_*,x_*,\delta,\frac{|\vec{k}-\vec{p}|}{k},\frac{p}{k}\right]\hat{\mathcal{O}}_-(\vec{k}-\vec{p})\hat{\mathcal{O}}_-(\vec{p}),\end{aligned} \tag{D3}$$

where we defined the product of helicity vectors

$$\epsilon_\lambda[\vec{k},\vec{k}-\vec{p},\vec{p}] \equiv \epsilon_i^\lambda(\vec{k})^*\epsilon_i^-(\vec{k}-\vec{p})\epsilon_j^\lambda(\vec{k})^*\epsilon_j^-(\vec{p}) \tag{D4}$$

and

$$\mathcal{I}_h[\xi_*, x_*, \delta, \tilde{p}, \tilde{q}] \equiv \mathcal{I}_h^{(1)}[\xi_*, x_*, \delta, \sqrt{\tilde{p}} + \sqrt{\tilde{q}}] + \frac{\sqrt{\tilde{p}\,\tilde{q}}}{2}\mathcal{I}_h^{(2)}[\xi_*, x_*, \delta, \sqrt{\tilde{p}} + \sqrt{\tilde{q}}], \tag{D5}$$

where $\mathcal{I}_h^{(1)}$ and $\mathcal{I}_h^{(2)}$ contain temporal integration of the gauge field sources [40,41]

$$\begin{aligned}
\mathcal{I}_h^{(1)}[\xi_*, x_*, \delta, Q] &\equiv \int_0^\infty \mathrm{d}x'(x'\cos x' - \sin x')\sqrt{\frac{\xi(x')}{x'}}\exp\left[-E(x')\sqrt{2\xi_* x'}Q\right], \\
\mathcal{I}_h^{(2)}[\xi_*, x_*, \delta, Q] &\equiv \int_0^\infty \mathrm{d}x'(x'\cos x' - \sin x')\sqrt{\frac{x'}{\xi(x')}}\exp\left[-E(x')\sqrt{2\xi_* x'}Q\right].
\end{aligned} \tag{D6}$$

Note that for the sourced scalar and tensor perturbations, the dependence of $\xi(x)$ and $E(x)$ on the axion potential in the spectator sector are provided in (2.7) and (A2), respectively.

1. STT and TSS bispectrum

Noting the definitions of the mixed bispectra in (3.1), we are ready to calculate $\langle \mathcal{R} h_\lambda h_\lambda \rangle$ and $\langle h_\lambda \mathcal{R}\mathcal{R} \rangle$ using $\hat{h}_\lambda$ (D3) and $\hat{\mathcal{R}}$ (D1). For this purpose, we employ Wick's theorem to compute the products of $\hat{\mathcal{O}}_-$ operators to obtain the following form for the mixed bispectra:

$$\begin{aligned}
\mathcal{B}^{(s)}_{\mathcal{R}\lambda\lambda}(\vec{k}_1, \vec{k}_2, \vec{k}_3) &\simeq \frac{[\epsilon_\phi \mathcal{P}^{(v)}_{\mathcal{R}}]^3}{(k_1 k_2 k_3)^2} f^{(3)}_{\mathcal{R}\lambda\lambda}(\xi_*, \delta, x_*, x_2, x_3), \\
\mathcal{B}^{(s)}_{\lambda\mathcal{R}\mathcal{R}}(\vec{k}_1, \vec{k}_2, \vec{k}_3) &\simeq \frac{[\epsilon_\phi \mathcal{P}^{(v)}_{\mathcal{R}}]^3}{(k_1 k_2 k_3)^2} f^{(3)}_{\lambda\mathcal{R}\mathcal{R}}(\xi_*, \delta, x_*, x_2, x_3),
\end{aligned} \tag{D7}$$

where we used the standard vacuum contribution to the scalar power spectrum (2.9) to replace the factors of $(H/M_{\rm pl})^6$, and we have fixed $k_1 = k$, $k_2 = x_2 k$, and $k_3 = x_3 k$. As indicated by the diagrams in Fig. 2, mixed correlators arise as a result of a "loop" computation over the internal momentum that labels gauge field modes. Defining the rescaled internal momentum as $\vec{\tilde{p}} = \vec{p}/k$, we found that dimensionless $f^{(3)}$ functions that parametrize this computation are given by

$$\begin{aligned}
f^{(3)}_{\mathcal{R}\lambda\lambda} = \frac{192\pi^3\xi_*}{(x_2x_3)^{3/2}} &\int \mathrm{d}^3\tilde{p}\,\epsilon_{(\mathcal{R}\lambda\lambda)}[\vec{\tilde{p}}, \hat{k}_1, \hat{k}_2, \hat{k}_3]\sqrt{\tilde{p}|\hat{k}_1 - \vec{\tilde{p}}||\vec{\tilde{p}} + x_2\hat{k}_2|}\left(\sqrt{\tilde{p}} + \sqrt{|\hat{k}_1 - \vec{\tilde{p}}|}\right)N_A^2(\xi_*, \tilde{p}x_*, \delta)N_A^2(\xi_*, |\hat{k}_1 - \vec{\tilde{p}}|x_*, \delta) \\
&\times N_A^2(\xi_*, |\vec{\tilde{p}} + x_2\hat{k}_2|x_*, \delta)\mathcal{I}_{\mathcal{R}}\left[\xi_*, x_*, \delta, \sqrt{\tilde{p}} + \sqrt{|\hat{k}_1 - \vec{\tilde{p}}|}\right]\mathcal{I}_h\left[\xi_*, x_2x_*, \delta, \frac{\tilde{p}}{x_2}, \frac{|\vec{\tilde{p}} + x_2\hat{k}_2|}{x_2}\right] \\
&\times \mathcal{I}_h\left[\xi_*, x_3x_*, \delta, \frac{|\hat{k}_1 - \vec{\tilde{p}}|}{x_3}, \frac{|\vec{\tilde{p}} + x_2\hat{k}_2|}{x_3}\right],
\end{aligned} \tag{D8}$$

and

$$\begin{aligned}
f^{(3)}_{\lambda\mathcal{R}\mathcal{R}} = \frac{72\pi^{9/2}\xi_*^2}{(x_2x_3)^2} &\int \mathrm{d}^3\tilde{p}\,\epsilon_{(\lambda\mathcal{R}\mathcal{R})}[\vec{\tilde{p}}, \hat{k}_1, \hat{k}_2, \hat{k}_3]\left(\sqrt{\tilde{p}} + \sqrt{|\vec{\tilde{p}} + x_2\hat{k}_2|}\right)\left(\sqrt{|\vec{\tilde{p}} + x_2\hat{k}_2|} + \sqrt{|\hat{k}_1 - \vec{\tilde{p}}|}\right) \\
&\times \sqrt{\tilde{p}|\hat{k}_1 - \vec{\tilde{p}}||\vec{\tilde{p}} + x_2\hat{k}_2|}N_A^2(\xi_*, \tilde{p}x_*, \delta)N_A^2(\xi_*, |\hat{k}_1 - \vec{\tilde{p}}|x_*, \delta)N_A^2(\xi_*, |\vec{\tilde{p}} + x_2\hat{k}_2|x_*, \delta)\mathcal{I}_h[\xi_*, x_*, \delta, \tilde{p}, |\hat{k}_1 - \vec{\tilde{p}}|] \\
&\times \mathcal{I}_{\mathcal{R}}\left[\xi_*, x_2x_*, \delta, \frac{\sqrt{\tilde{p}} + \sqrt{|\vec{\tilde{p}} + x_2\hat{k}_2|}}{\sqrt{x_2}}\right]\mathcal{I}_{\mathcal{R}}\left[\xi_*, x_3x_*, \delta, \frac{\sqrt{|\hat{k}_1 - \vec{\tilde{p}}|} + \sqrt{|\vec{\tilde{p}} + x_2\hat{k}_2|}}{\sqrt{x_3}}\right].
\end{aligned} \tag{D9}$$

For the numerical evaluation of the integrals, keeping the definition (D4) in mind, we note the product of helicity vectors in (D8) and (D9) as

$$\begin{aligned}\epsilon_{(\mathcal{R}\lambda\lambda)} &\equiv \epsilon^{-}_{i}(\hat{k}_1-\vec{\tilde{p}})\epsilon^{-}_{i}(\vec{\tilde{p}})\epsilon_{\lambda}[\hat{k}_2,-\vec{\tilde{p}},\vec{\tilde{p}}+x_2\hat{k}_2]\epsilon_{\lambda}[\hat{k}_3,-(\hat{k}_1-\vec{\tilde{p}}),-(\vec{\tilde{p}}+x_2\hat{k}_2)],\\ \epsilon_{(\lambda\mathcal{R}\mathcal{R})} &\equiv \epsilon_{\lambda}[\hat{k}_1,\hat{k}_1-\vec{\tilde{p}},\vec{\tilde{p}}]\epsilon^{-}_{i}(-\vec{\tilde{p}})\epsilon^{-}_{i}(\vec{\tilde{p}}+x_2\hat{k}_2)\epsilon^{-}_{j}(-(\hat{k}_1-\vec{\tilde{p}}))\epsilon^{-}_{j}(-(\vec{\tilde{p}}+x_2\hat{k}_2)).\end{aligned} \tag{D10}$$

Finally, we align $\vec{k}_1$ along the x axis, $\vec{k}_1 = k(1,0,0)$ and express $\vec{k}_2$ and $\vec{k}_3$ in terms of x_2 and x_3,

$$\begin{aligned}\vec{k}_2 &= kx_2\left(\frac{-1-x_2^2+x_3^2}{2x_2},\frac{\sqrt{-(1-x_2+x_3)(1+x_2-x_3)(1-x_2-x_3)(1+x_2+x_3)}}{2x_2},0\right),\\ \vec{k}_3 &= kx_3\left(\frac{-1+x_2^2-x_3^2}{2x_3},-\frac{\sqrt{-(1-x_2+x_3)(1+x_2-x_3)(1-x_2-x_3)(1+x_2+x_3)}}{2x_3},0\right),\end{aligned} \tag{D11}$$

and define the polarization vector for a given momentum $\vec{q}$ in terms of its components as

$$\epsilon^{\lambda}(\vec{q}) = \frac{1}{\sqrt{2}}\left(\frac{q_x q_z - i\lambda q_y|\vec{q}|}{|\vec{q}|\sqrt{q_x^2+q_y^2}},\frac{q_y q_z + i\lambda q_x|\vec{q}|}{|\vec{q}|\sqrt{q_x^2+q_y^2}},-\frac{\sqrt{q_x^2+q_y^2}}{|\vec{q}|}\right). \tag{D12}$$

The shape and scale dependence of the $f^{(3)}$ functions can then be obtained numerically by fixing the background parameters $\{\xi_*,\delta\}$ that parametrize the efficiency of the particle production process in the gauge field sector.

2. Properties of the mixed bispectra

Let us verify some basic properties of the mixed bispectra (D7) we derived here. To show the invariance of $\mathcal{B}_j$ under the exchange of $\vec{k}_2 \leftrightarrow \vec{k}_3$, we first replace $\vec{k}_2 \to \vec{k}_3$ and $\vec{k}_3 \to \vec{k}_2$ on both sides of the expressions in (D7) using (D8)–(D10). Then, changing the integration variable $\vec{p} \to -\vec{p} + \vec{k}_1$ and noting $\sum_i \vec{k}_i = 0$, it is easy confirm that the resulting expressions are equivalent to (D9) and (D8). To prove that $\mathcal{B}_j$ is real, we first use the reality of h_{ij} and $\mathcal{R}$ in the configuration space, which implies $h_\lambda(\vec{k}) = h^*_\lambda(-\vec{k})$ and $\mathcal{R}(\vec{k}) = \mathcal{R}^*(-\vec{k})$. Using the last two identities, then $\mathcal{B}_j(\vec{k}_1,\vec{k}_2,\vec{k}_3) = \mathcal{B}^*_j(-\vec{k}_1,-\vec{k}_2,-\vec{k}_3)$ follows immediately. Finally, focusing on the latter quantity, we perform a 180° rotation around the axis $\perp$ to the plane defined by $\sum_i \vec{k}_i = 0$ to change the orientation of the external momenta $-\vec{k}_i \to \vec{k}_i$ in its arguments and note the invariance of the bispectrum under this action due to isotropy of the background, which together implies $\mathcal{B}^*_j(-\vec{k}_1,-\vec{k}_2,-\vec{k}_3) = \mathcal{B}^*_j(\vec{k}_1,\vec{k}_2,\vec{k}_3)$ and hence, $\mathcal{B}_j(\vec{k}_1,\vec{k}_2,\vec{k}_3) = \mathcal{B}^*_j(\vec{k}_1,\vec{k}_2,\vec{k}_3)$. From these arguments, we also infer the following relation: $\mathcal{B}_j(-\vec{k}_1,-\vec{k}_2,-\vec{k}_3) = \mathcal{B}_j(\vec{k}_1,\vec{k}_2,\vec{k}_3)$.

3. Peak structure of $f^{(3)}_{-\mathcal{R}\mathcal{R}}$ vs $f^{(3)}_{\mathcal{R}--}$ at the equilateral configuration

To understand the peak structure of the mixed $-\mathcal{R}\mathcal{R}$ and $\mathcal{R}--$ correlators, we focus our attention on the integrands of Eqs. (D8) and (D9) at the equilateral configuration $x_2 = x_3 = 1$. The integrands depend on the magnitude of momentum $\tilde{p}$ running in the loop (see Fig. 2), and its orientation—parametrized by the polar θ and azimuthal angle ϕ—with respect to the plane (x-y) where external momenta $\vec{k}_i$ live [see Eq. (D11)]. At fixed δ, their structure can be schematically written as

$$If^{(3)}_{j}(\xi_*,x_*,\tilde{p},\theta,\phi) \propto \underbrace{\epsilon_{(j)}[\vec{\tilde{p}},\vec{k}_1,\vec{k}_2,\vec{k}_3]}_{(a)}\underbrace{\mathcal{I}_h(\ldots)\mathcal{I}_{h/\mathcal{R}}(\ldots)\mathcal{I}_{\mathcal{R}}(\ldots)}_{(b)}\underbrace{N^c_A[\xi_*]^6\tilde{p}^n e^{-\frac{3}{\sigma_A[\xi_*]^2}\ln^2\left(\frac{\tilde{p}x_*}{q^c_A[\xi_*]}\right)}}_{(c)}, \tag{D13}$$

where $n = \{4, 9/2\}$ for the $\mathcal{R}--$ and $-\mathcal{R}\mathcal{R}$ correlators, respectively. We discuss the physical implications of the parts contributing to the integrand (D13) below.

(i) (c): These terms identify the scale-dependent amplitudes of gauge field mode functions in (A3) and the manifestly $\tilde{p}$-dependent terms using the second and first lines of the loop integrals in (D8) and (D9). Physically, they characterize the scale-dependent $x_* = k_i/k_* = k/k_*$ enhancement of the gauge modes running in the internal lines whose overall amplitude is dictated by the normalization factors $N^c_A[\xi_*]^6$ (see Table III). Notice that, in writing these terms, we ignored their θ and ϕ dependence in the $\tilde{p}^n \exp[\ldots]$ part, as the orientation of the loop momentum with respect to the plane of external momenta has a slight impact on the overall amplitude of

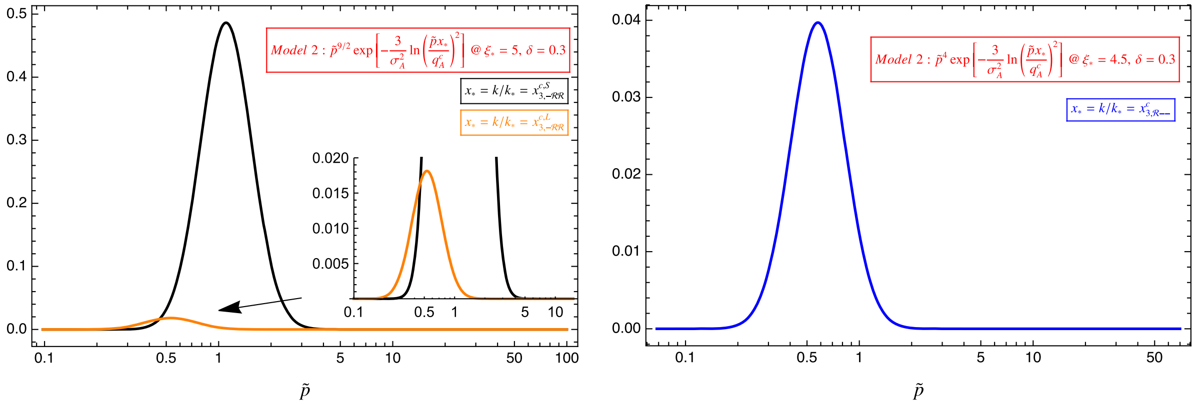

FIG. 8. Dependence of the amplified gauge field modes on the magnitude of loop momentum $\tilde{p}$ for $-\mathcal{R}\mathcal{R}$ (left) and $\mathcal{R}--$ (right). Both plots are normalized with $N_A^c[\xi_*]^6$; see, e.g., (c) in (D13).

gauge field modes compared to $\tilde{p}$. An essential feature of the terms labeled by (c) is that they acquire a peak (with an amplitude set by the $N_A^c[\xi_*]^6$ factor) located at

$$\tilde{p}_{\rm peak}x_* = e^{\frac{n\sigma_A[\xi_*]^2}{6}}q_A^c[\xi_*], \tag{D14}$$

which is important for understanding the scale dependence of the mixed correlators. In particular, (D14) implies that for larger (smaller) $x_* = k/k_*$, the loop integrals that characterize the correlators will have support around smaller (larger) values of $\tilde{p}_{\rm peak}$ because for $\tilde{p} > \tilde{p}_{\rm peak}$ or $\tilde{p} < \tilde{p}_{\rm peak}$, the terms labeled by (c) decay away quickly due to their exponential dependence. We illustrate these facts in Fig. 8 where we plot the terms labeled by (c) as a function of the magnitude of loop momentum $\tilde{p}$ for both correlators that we focus on and for different k/k_*.

(ii) (b): The product of integrals $\mathcal{I}_{h/\mathcal{R}}$ in (D13) captures the propagation of the amplified gauge modes from the internal lines to the external lines characterized by the late-time curvature $\mathcal{R}$ or tensor perturbation h through the vertices shown in Fig. 2. For the purpose of understanding the peak structure of the mixed correlators we are interested in, we plot them in Fig. 9 in terms of $\tilde{p}$ for different x_* and loop momentum configurations. We observe that for the range of $\tilde{p}$ values where the gauge field modes have appreciable contribution to the correlators (see Fig. 8), the propagation effects associated with tensors are always negative $\mathcal{I}_h < 0$, whereas for the curvature perturbation, the same quantity is strictly positive $\mathcal{I}_{\mathcal{R}} > 0$. We found that this conclusion holds irrespective of the choice of loop momentum configurations parametrized by the polar θ and azimuthal angle ϕ.

(iii) (a): These terms represent the scalar product of polarization vectors defined by (D10) and (D4) in the equilateral configuration $x_2 = x_3 = 1$ and serve the purpose of helicity conservation at each vertex. Their behavior with respect to the magnitude of the loop momentum $\tilde{p}$ is crucial in understanding the double-peak vs single-peak structure of the $-\mathcal{R}\mathcal{R}$ and

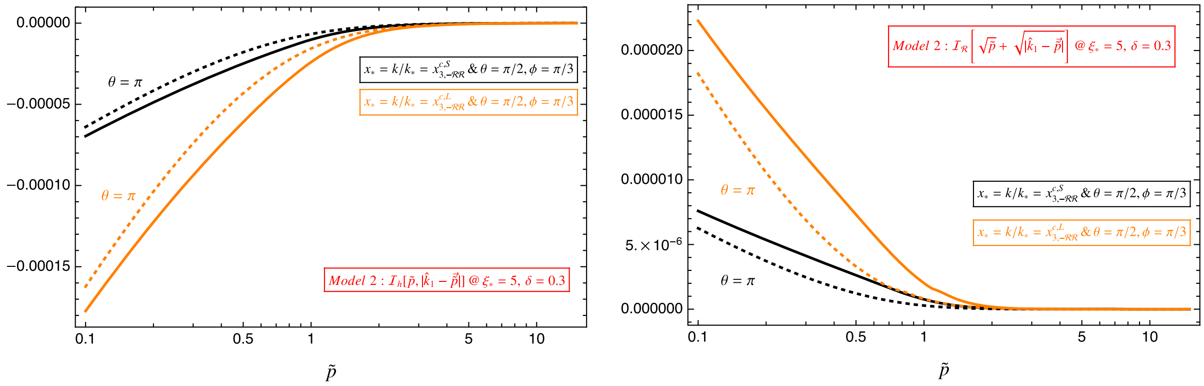

FIG. 9. Dependence of the $\mathcal{I}_{h/\mathcal{R}}$ [Eqs. (D5), (D6), and (D2)] on the magnitude of loop momentum $\tilde{p}$.

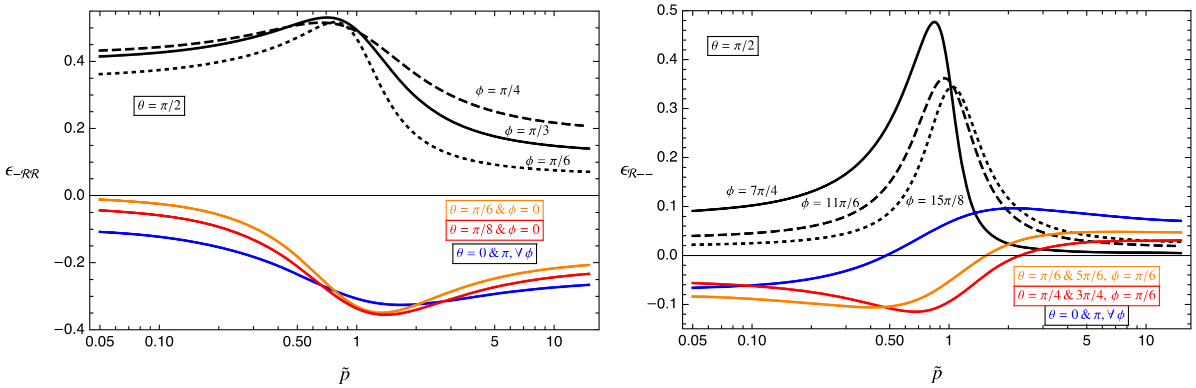

FIG. 10. The product of helicity vectors defined in (D10) for $x_2 = x_3 = 1$ as a function of $\tilde{p}$ and for different loop momentum orientation with respect to the plane of external momenta $\vec{k}_i$. In both panels, the maximal positive contributions to the product arise when the loop momentum lies in the x-y plane, namely, when $\theta = \pi/2$.

$\mathcal{R}--$ correlators as we explain below. For orientations of loop momentum that leads to maximal results, we show the behavior of $\epsilon_{(-\mathcal{R}\mathcal{R})}[\vec{p}, \vec{k}_1, \vec{k}_2, \vec{k}_3]$ and $\epsilon_{(\mathcal{R}--)}[\vec{p}, \vec{k}_1, \vec{k}_2, \vec{k}_3]$ as a function of $\tilde{p}$ in Fig. 10.

From the left panel of Fig. 10, we see that $\epsilon_{(-\mathcal{R}\mathcal{R})}$ has a significant negative support for loop momentum configurations that does not lie in the x-y plane ($\theta \neq \pi/2$) in the $\tilde{p} \gtrsim 1$ regime. In this region, the integrand (D13) of the $-\mathcal{R}\mathcal{R}$ correlator (D9) has significant support from the amplified gauge field mode functions at small k/k_* (black curve in the left panel of Fig. 8), and integrating it over such loop momentum configurations leads to a positive peak at small $k/k_* = x^{c,S}_{3,-\mathcal{R}\mathcal{R}}$, recalling the overall negative sign of propagation effects $\mathcal{I}_h\mathcal{I}_\mathcal{R}\mathcal{I}_\mathcal{R} < 0$. On the other hand, for loop momentum that lives in the same plane with the external momenta ($\theta = \pi/2$), the product of the polarization vectors has a positive support in the $\tilde{p} \lesssim 1$ region. In this regime, the integrand (D13) still has support from the peak of the amplified gauge field modes at larger $k/k_* = x^{c,L}_{3,-\mathcal{R}\mathcal{R}}$ (orange curve in the left panel of Fig. 8). Therefore, the $-\mathcal{R}\mathcal{R}$ correlator obtains a second peak occurring in the negative direction due to the overall negative contributions that arise from the propagation effects $\mathcal{I}_h\mathcal{I}_\mathcal{R}\mathcal{I}_\mathcal{R} < 0$.

For the $\mathcal{R}--$ correlator, setting the product of polarization vectors aside, the integrand (D13) has an overall positive sign due to propagation effects $\mathcal{I}_\mathcal{R}\mathcal{I}_h\mathcal{I}_h > 0$. More importantly, contrary to the case of the $-\mathcal{R}\mathcal{R}$ correlator, the range of loop momenta $\tilde{p} \lesssim 1$, where the amplified gauge field modes can contribute to the integrand (see the right panel in Fig. 8), overlaps with the range where the product of helicity vectors takes its maximal values which is positive for $\theta = \pi/2$ as can be seen from Fig. 10. Integrating (D13) over such configurations therefore leads to a single peak for the $\mathcal{R}--$ correlator (D8) occurring in the positive direction as the dominant support for $\epsilon_{(\mathcal{R}--)}$ is positive in this regime.

Considering that the $-\mathcal{R}\mathcal{R}$ and $\mathcal{R}--$ correlators differ from each other by an external scalar/ tensor state ($\mathcal{R}/h$) and comparing the left/right panel of Fig. 10, we can physically make sense of these results. In particular, for large enough transverse momentum $\tilde{p} \gtrsim 1$, conservation of angular momentum allows two internal photons to generate an external scalar perturbation $\mathcal{R}$ even if the latter lies in a plane different from the internal photons ($\theta \neq \pi/2$). In this way, one can generate soft $\mathcal{R}$'s to induce sizeable correlations between external states of $-\mathcal{R}\mathcal{R}$ in the form of an early peak located at $k_i/k_* = k/k_* = x^{c,S}_{3,-\mathcal{R}\mathcal{R}} < x^{c,L}_{3,-\mathcal{R}\mathcal{R}}$ (see Fig. 3). On the other hand, for soft internal momenta $\tilde{p} \lesssim 1$, internal photon states can still induce sizeable correlations between the external states of the $-\mathcal{R}\mathcal{R}$ correlator as far as the external momentum $\vec{k}_i$ lies in the same plane with the loop momentum $\vec{p}$ ($\theta = \pi/2$). Since the loop momentum does not leak beyond the plane of external momenta in this case, a sizeable $-\mathcal{R}\mathcal{R}$ correlation can be induced at harder external momenta satisfying $k_i/k_* = k/k_* = x^{c,L}_{3,-\mathcal{R}\mathcal{R}} > x^{c,S}_{3,-\mathcal{R}\mathcal{R}}$, explaining the presence of a second peak in the $-\mathcal{R}\mathcal{R}$ correlator (see Fig. 3). However, as can be seen from the right panel of Fig. 10, the same situation is more restrictive if the external state is a graviton. In this case, angular momentum conservation strictly prefers the production of an external graviton from two internal photons (preferably soft $\tilde{p} \lesssim 1$) that lie in the same plane, and the resulting correlation between the external states of the $\mathcal{R}--$ correlator is thus maximal at a single location parametrized by $k_i/k_* = x^c_{3,\mathcal{R}--}$. In light of the discussion above, we conclude that the product of the polarization vectors is the key quantity that determines the double-peak vs single-peak structure of mixed correlators.

APPENDIX E: APPROXIMATE FACTORIZED FORMS FOR THE MIXED BISPECTRA

We now derive factorized approximate expressions for the STT (D8) and TSS (D9) bispectrum as a sum of terms given by the products of sourced signals $f_{2,j}(k_i)$ and $f^{(3)}_j(k_i,k_i,k_i)$ that contains only a single external momenta k_i.

(i) STT: Similar to the three autocorrelators, we expect that the mixed spectra have a peaked structure so that we can utilize the two-point and three-point correlators (evaluated at the equilateral configuration) to describe it in a factorized form. Motivated by these considerations and the $\vec{k}_2 \leftrightarrow \vec{k}_3$ symmetry of the STT bispectrum, we start with the following ansatz:

$$f^{(3,\mathrm{app})}_{\mathcal{R}\lambda\lambda} \simeq \mathcal{C}\left\{\frac{f^{(3)}_{\mathcal{R}\lambda\lambda}(s_1k_1,s_1k_1,s_1k_1)}{f_{2,\mathcal{R}}(\bar{s}_1k_1)^{1/2}f_{2,\lambda}(\tilde{s}_1k_1)} + \left[\frac{f^{(3)}_{\mathcal{R}\lambda\lambda}(s_2k_2,s_2k_2,s_2k_2)}{f_{2,\mathcal{R}}(\bar{s}_2k_2)^{1/2}f_{2,\lambda}(\tilde{s}_2k_2)} + k_2 \to k_3\right]\right\}\prod_{i=2,3}[f_{2,\mathcal{R}}(\bar{s}_1k_1)f_{2,\lambda}(\tilde{s}_2k_i)]^{1/2}, \tag{E1}$$

where we introduced scaling factors for the external momenta in the sourced quantities $f_{2,j}$ and $f^{(3)}_j$ to be able to locate the maximum of the bispectra accurately in the $k_1 - k_2$ (recall that we focus on isosceles triangles $k_2 = k_3$). $\mathcal{C}$ is an overall coefficient that we will fix to reproduce the correct normalization of the exact bispectra as we describe below.

To ensure that the approximate expression (E1) describes the actual one accurately around its maximum, we can utilize the peak locations of the two-point functions $x^c_{2,j}$ (see Table IV) and three-point functions evaluated at the equilateral configuration $x^c_{3,\mathcal{R}\lambda\lambda}$ (see Table II). In particular, since we know (by numerical evaluation) the triangle configuration at which the exact bispectra is maximal, say, at $k_{1,2} = k^m_{1,2}$, we can fix the scaling factors $s, \bar{s}, \tilde{s}$ in (E1) appropriately as $s_{1,2} = x^c_{3,j}/k^m_{1,2}$, $\bar{s}_{1,2} = x^c_{2,\mathcal{R}}/k^m_{1,2}$, and $\tilde{s}_{1,2} = x^c_{2,\lambda}/k^m_{1,2}$ for a given set of model parameters ξ_* and δ. Considering the Gaussian forms of the two-point (2.10) and three-point mixed correlators [see, e.g., (3.3)], the aforementioned choices of scaling factors provide a very accurate guess for the exact location of the maximum in the $k_1 - k_2$ plane. To fix the overall normalization $\mathcal{C}$, we then enforce the approximate expression (E1) at its maximum to be equal to the maximum of the exact one derived from (D8), i.e., $f^{3,\max}_{\mathcal{R}\lambda\lambda} = f^{(3)}_{\mathcal{R}\lambda\lambda}(k^m_1, k^m_2)$.

(ii) TSS: For the TSS-type correlators, following the same procedures above, we found that the following expression provides an accurate description of the exact bispectrum:

$$f^{(3,\mathrm{app})}_{\lambda\mathcal{R}\mathcal{R}} \simeq \mathcal{D}\left\{\frac{f^{(3)}_{\lambda\mathcal{R}\mathcal{R}}(s_1k_1,s_1k_1,s_1k_1)}{f_{2,\lambda}(\tilde{s}_1k_1)^{3/2}} + \left[\frac{f^{(3)}_{\lambda\mathcal{R}\mathcal{R}}(s_2k_2,s_2k_2,s_2k_2)}{f_{2,\mathcal{R}}(\bar{s}_2k_2)^{3/2}} + k_2 \to k_3\right]\right\}\prod_{i=2,3}[f_{2,\lambda}(\tilde{s}_1k_1)f_{2,\mathcal{R}}(\bar{s}_2k_i)]^{1/2}, \tag{E2}$$

where $s_{1,2} = x^c_{3,\lambda\mathcal{R}\mathcal{R}}/k^m_{1,2}$, $\tilde{s}_1 = x^c_{2,\lambda}/k^m_1$, and $\bar{s}_2 = x^c_{2,\mathcal{R}}/k^m_2$. Using Tables IV and I for a given set of model parameters ξ_* and δ, one can fix the overall coefficient $\mathcal{D}$ by matching the approximate expression (E2) at its maximum to the exact bispectrum at the triangle configuration where it peaks, i.e., $f^{3,\max}_{\lambda\mathcal{R}\mathcal{R}} = f^{(3)}_{\lambda\mathcal{R}\mathcal{R}}(k^m_1, k^m_2)$. For $\delta = 0.3$ and $\xi_* = 5$, the accuracy of (E1) and (E2) derived through the procedure we described above is shown in the top and bottom panels of Fig. 6. Since this process does not require a specific choice of the model parameters, we anticipate that it will also generate accurate factorized forms of the mixed bispectra for other choices of model parameters δ, ξ_*.

[1] M. C. Guzzetti, N. Bartolo, M. Liguori, and S. Matarrese, Gravitational waves from inflation, Riv. Nuovo Cimento **39**, 399 (2016).

[2] C. Caprini and D. G. Figueroa, Cosmological backgrounds of gravitational waves, Classical Quantum Gravity **35**, 163001 (2018).

[3] A. H. Guth, The inflationary universe: A possible solution to the horizon and flatness problems, Phys. Rev. D **23**, 347 (1981).

[4] A. D. Linde, A new inflationary universe scenario: A possible solution of the horizon, flatness, homogeneity, isotropy and primordial monopole problems, Phys. Lett. **108B**, 389 (1982).

[5] D. Baumann, Inflation, Physics of the large and the small, in *Proceedings of the Theoretical Advanced Study Institute in Elementary Particle Physics, TASI 09, Boulder, Colorado, 2009* (2011), pp. 523–686, arXiv:0907.5424, 10.1142/9789814327183_0010.

[6] M. Zaldarriaga and U. Seljak, An all sky analysis of polarization in the microwave background, Phys. Rev. D **55**, 1830 (1997).

[7] M. Kamionkowski, A. Kosowsky, and A. Stebbins, Statistics of cosmic microwave background polarization, Phys. Rev. D **55**, 7368 (1997).

[8] M. Kamionkowski and E. D. Kovetz, The quest for B modes from inflationary gravitational waves, Annu. Rev. Astron. Astrophys. **54**, 227 (2016).

[9] P. A. R. Ade *et al.* (BICEP2, Keck Array Collaborations), Improved Constraints on Cosmology and Foregrounds from BICEP2 and Keck Array Cosmic Microwave Background Data with Inclusion of 95 GHz Band, Phys. Rev. Lett. **116**, 031302 (2016).

[10] Y. Akrami *et al.* (Planck Collaboration), Planck 2018 results. X. Constraints on inflation, Astron. Astrophys. **641**, A10 (2020).

[11] K. N. Abazajian *et al.* (CMB-S4 Collaboration), CMB-S4 Science Book, 1st ed., arXiv:1610.02743.

[12] M. Hazumi *et al.*, LiteBIRD: A satellite for the studies of B-mode polarization and inflation from cosmic background radiation detection, J. Low Temp. Phys. **194**, 443 (2019).

[13] M. Mylova, O. Özsoy, S. Parameswaran, G. Tasinato, and I. Zavala, A new mechanism to enhance primordial tensor fluctuations in single field inflation, J. Cosmol. Astropart. Phys. 12 (2018) 024.

[14] O. Ozsoy, M. Mylova, S. Parameswaran, C. Powell, G. Tasinato, and I. Zavala, Squeezed tensor non-Gaussianity in non-attractor inflation, J. Cosmol. Astropart. Phys. 09 (2019) 036.

[15] S. Alexander and J. Martin, Birefringent gravitational waves and the consistency check of inflation, Phys. Rev. D **71**, 063526 (2005).

[16] M. Satoh and J. Soda, Higher curvature corrections to primordial fluctuations in slow-roll inflation, J. Cosmol. Astropart. Phys. 09 (2008) 019.

[17] J. L. Cook and L. Sorbo, Particle production during inflation and gravitational waves detectable by ground-based interferometers, Phys. Rev. D **85**, 023534 (2012).

[18] L. Senatore, E. Silverstein, and M. Zaldarriaga, New sources of gravitational waves during inflation, J. Cosmol. Astropart. Phys. 08 (2014) 016.

[19] D. Baumann and L. McAllister, *Inflation and String Theory* (Cambridge University Press, Cambridge, England, 2015).

[20] B. Ratra, Cosmological "seed" magnetic field from inflation, Astrophys. J. Lett. **391**, L1 (1992).

[21] W. D. Garretson, G. B. Field, and S. M. Carroll, Primordial magnetic fields from pseudo Goldstone bosons, Phys. Rev. D **46**, 5346 (1992).

[22] M. M. Anber and L. Sorbo, Naturally inflating on steep potentials through electromagnetic dissipation, Phys. Rev. D **81**, 043534 (2010).

[23] P. Adshead and M. Wyman, Chromo-Natural Inflation: Natural Inflation on a Steep Potential with Classical Non-Abelian Gauge Fields, Phys. Rev. Lett. **108**, 261302 (2012).

[24] G. Dall'Agata, Chromo-natural inflation in supergravity, Phys. Lett. B **782**, 139 (2018).

[25] E. McDonough and S. Alexander, Observable chiral gravitational waves from inflation in string theory, J. Cosmol. Astropart. Phys. 11 (2018) 030.

[26] J. Holland, I. Zavala, and G. Tasinato, On chromonatural inflation in string theory, J. Cosmol. Astropart. Phys. 12 (2020) 026.

[27] N. Barnaby and M. Peloso, Large Non-Gaussianity in Axion Inflation, Phys. Rev. Lett. **106**, 181301 (2011).

[28] N. Barnaby, R. Namba, and M. Peloso, Phenomenology of a pseudo-scalar inflaton: Naturally large nongaussianity, J. Cosmol. Astropart. Phys. 04 (2011) 009.

[29] N. Barnaby, R. Namba, and M. Peloso, Observable non-Gaussianity from gauge field production in slow roll inflation, and a challenging connection with magnetogenesis, Phys. Rev. D **85**, 123523 (2012).

[30] M. M. Anber and L. Sorbo, Non-Gaussianities and chiral gravitational waves in natural steep inflation, Phys. Rev. D **85**, 123537 (2012).

[31] A. Linde, S. Mooij, and E. Pajer, Gauge field production in supergravity inflation: Local non-Gaussianity and primordial black holes, Phys. Rev. D **87**, 103506 (2013).

[32] E. Bugaev and P. Klimai, Axion inflation with gauge field production and primordial black holes, Phys. Rev. D **90**, 103501 (2014).

[33] E. Erfani, Primordial black holes formation from particle production during inflation, J. Cosmol. Astropart. Phys. 04 (2016) 020.

[34] J. Garcia-Bellido, M. Peloso, and C. Unal, Gravitational waves at interferometer scales and primordial black holes in axion inflation, J. Cosmol. Astropart. Phys. 12 (2016) 031.

[35] V. Domcke, F. Muia, M. Pieroni, and L. T. Witkowski, PBH dark matter from axion inflation, J. Cosmol. Astropart. Phys. 07 (2017) 048.

[36] O. Özsoy and Z. Lalak, Primordial black holes as dark matter and gravitational waves from bumpy axion inflation, J. Cosmol. Astropart. Phys. 01 (2021) 040.

[37] J. P. B. Almeida, N. Bernal, D. Bettoni, and J. Rubio, Chiral gravitational waves and primordial black holes in UV-protected Natural Inflation, J. Cosmol. Astropart. Phys. 11 (2020) 009.

[38] O. Özsoy, K. Sinha, and S. Watson, How well can we really determine the scale of inflation?, Phys. Rev. D **91**, 103509 (2015).

[39] M. Mirbabayi, L. Senatore, E. Silverstein, and M. Zaldarriaga, Gravitational waves and the scale of inflation, Phys. Rev. D **91**, 063518 (2015).

[40] R. Namba, M. Peloso, M. Shiraishi, L. Sorbo, and C. Unal, Scale-dependent gravitational waves from a rolling axion, J. Cosmol. Astropart. Phys. 01 (2016) 041.

[41] O. Özsoy, Synthetic gravitational waves from a rolling axion monodromy, J. Cosmol. Astropart. Phys. 04 (2021) 040.

[42] N. Barnaby, J. Moxon, R. Namba, M. Peloso, G. Shiu, and P. Zhou, Gravity waves and non-Gaussian features from particle production in a sector gravitationally coupled to the inflaton, Phys. Rev. D **86**, 103508 (2012).

[43] S. Mukohyama, R. Namba, M. Peloso, and G. Shiu, Blue tensor spectrum from particle production during inflation, J. Cosmol. Astropart. Phys. 08 (2014) 036.

[44] R. Z. Ferreira and M. S. Sloth, Universal constraints on axions from inflation, J. High Energy Phys. 12 (2014) 139.

[45] O. Özsoy, On synthetic gravitational waves from multi-field inflation, J. Cosmol. Astropart. Phys. 04 (2018) 062.

[46] A. Lue, L.-M. Wang, and M. Kamionkowski, Cosmological Signature of New Parity Violating Interactions, Phys. Rev. Lett. **83**, 1506 (1999).

[47] S. Saito, K. Ichiki, and A. Taruya, Probing polarization states of primordial gravitational waves with CMB anisotropies, J. Cosmol. Astropart. Phys. 09 (2007) 002.

[48] V. Gluscevic and M. Kamionkowski, Testing parity-violating mechanisms with cosmic microwave background experiments, Phys. Rev. D **81**, 123529 (2010).

[49] A. Ferté and J. Grain, Detecting chiral gravity with the pure pseudospectrum reconstruction of the cosmic microwave background polarized anisotropies, Phys. Rev. D **89**, 103516 (2014).

[50] M. Gerbino, A. Gruppuso, P. Natoli, M. Shiraishi, and A. Melchiorri, Testing chirality of primordial gravitational waves with Planck and future CMB data: No hope from angular power spectra, J. Cosmol. Astropart. Phys. 07 (2016) 044.

[51] M. Shiraishi, C. Hikage, R. Namba, T. Namikawa, and M. Hazumi, Testing statistics of the CMB B-mode polarization toward unambiguously establishing quantum fluctuation of the vacuum, Phys. Rev. D **94**, 043506 (2016).

[52] E. Dimastrogiovanni, M. Fasiello, R. J. Hardwick, H. Assadullahi, K. Koyama, and D. Wands, Non-Gaussianity from axion-gauge fields interactions during inflation, J. Cosmol. Astropart. Phys. 11 (2018) 029.

[53] T. Fujita, R. Namba, and I. Obata, Mixed non-Gaussianity from axion-gauge field dynamics, J. Cosmol. Astropart. Phys. 04 (2019) 044.

[54] N. Bartolo and G. Orlando, Parity breaking signatures from a Chern-Simons coupling during inflation: The case of non-Gaussian gravitational waves, J. Cosmol. Astropart. Phys. 07 (2017) 034.

[55] N. Bartolo, G. Orlando, and M. Shiraishi, Measuring chiral gravitational waves in Chern-Simons gravity with CMB bispectra, J. Cosmol. Astropart. Phys. 01 (2019) 050.

[56] M. Peloso, L. Sorbo, and C. Unal, Rolling axions during inflation: Perturbativity and signatures, J. Cosmol. Astropart. Phys. 09 (2016) 001.

[57] K. Freese, J. A. Frieman, and A. V. Olinto, Natural Inflation with Pseudo–Nambu-Goldstone Bosons, Phys. Rev. Lett. **65**, 3233 (1990).

[58] L. McAllister, E. Silverstein, and A. Westphal, Gravity waves and linear inflation from axion monodromy, Phys. Rev. D **82**, 046003 (2010).

[59] L. McAllister, E. Silverstein, A. Westphal, and T. Wrase, The powers of monodromy, J. High Energy Phys. 09 (2014) 123.

[60] L. Sorbo, Parity violation in the cosmic microwave background from a pseudoscalar inflaton, J. Cosmol. Astropart. Phys. 06 (2011) 003.

[61] B. Thorne, T. Fujita, M. Hazumi, N. Katayama, E. Komatsu, and M. Shiraishi, Finding the chiral gravitational wave background of an axion-SU(2) inflationary model using CMB observations and laser interferometers, Phys. Rev. D **97**, 043506 (2018).

[62] A. Agrawal, T. Fujita, and E. Komatsu, Large tensor non-Gaussianity from axion-gauge field dynamics, Phys. Rev. D **97**, 103526 (2018).

[63] A. Agrawal, T. Fujita, and E. Komatsu, Tensor non-Gaussianity from axion-gauge-fields dynamics: Parameter search, J. Cosmol. Astropart. Phys. 06 (2018) 027.

[64] S. Eccles, W. Fischler, D. Lorshbough, and B. A. Stephens, Vector field instability and the primordial tensor spectrum, arXiv:1505.04686.

[65] E. Komatsu and D. N. Spergel, Acoustic signatures in the primary microwave background bispectrum, Phys. Rev. D **63**, 063002 (2001).

[66] J. M. Maldacena, Non-Gaussian features of primordial fluctuations in single field inflationary models, J. High Energy Phys. 05 (2003) 013.

[67] D. Babich, P. Creminelli, and M. Zaldarriaga, The shape of non-Gaussianities, J. Cosmol. Astropart. Phys. 08 (2004) 009.

[68] J. R. Fergusson and E. P. S. Shellard, The shape of primordial non-Gaussianity and the CMB bispectrum, Phys. Rev. D **80**, 043510 (2009).

[69] E. Dimastrogiovanni, M. Fasiello, and T. Fujita, Primordial gravitational waves from axion-gauge fields dynamics, J. Cosmol. Astropart. Phys. 01 (2017) 019.

[70] T. Fujita, R. Namba, and Y. Tada, Does the detection of primordial gravitational waves exclude low energy inflation?, Phys. Lett. B **778**, 17 (2018).

[71] M. Shiraishi, Parity violation of primordial magnetic fields in the CMB bispectrum, J. Cosmol. Astropart. Phys. 06 (2012) 015.

[72] M. Shiraishi, Polarization bispectrum for measuring primordial magnetic fields, J. Cosmol. Astropart. Phys. 11 (2013) 006.

[73] G. Domènech, T. Hiramatsu, C. Lin, M. Sasaki, M. Shiraishi, and Y. Wang, CMB scale dependent non-Gaussianity from massive gravity during inflation, J. Cosmol. Astropart. Phys. 05 (2017) 034.